Upper ocean heat and freshwater budgets in the eastern Pacific warm pool

Hemantha W. Wijesekera,[1] Daniel L. Rudnick,[2] Clayton A. Paulson,[1] Stephen D. Pierce,[1] W. Scott Pegau,[3] John Mickett,[4] and Michael C. Gregg[4]

Received 28 May 2004; revised 23 February 2005; accepted 18 March 2005; published 11 August 2005.

[1] This study focuses on upper ocean budgets of heat and freshwater, which yield estimates of net surface heat flux and rainfall minus evaporation. The budgets are based on a 19 day ship survey conducted as part of the Eastern Pacific Investigation of Climate Processes in the Coupled Ocean-Atmosphere System 2001 in September 2001. Underway measurements included temperature and salinity sections from an undulating platform, SeaSoar, and horizontal currents from an acoustic Doppler current profiler along a 146 × 146 km survey pattern centered near 10°N, 95°W in the eastern Pacific warm pool. Additional measurements from a second ship at the center of the survey pattern included radar backscatter from rainfall, air-sea fluxes, and vertical profiles of temperature, salinity, microstructure, and horizontal velocity. Satellite measurements of surface height, temperature, and rainfall were also analyzed. The heat budget of 20 and 25 m surface layers indicated that storage, advection, turbulent transport, and penetrative solar radiation were all significant components of the heat budget with a net surface cooling of 41 W m^{-2} estimated as a residual, which agreed with atmospheric measurements (30 W m^{-2}). The precipitation rate from the freshwater budget was 29 mm d^{-1}, which was in excellent agreement with in situ measurements on both ships and in good agreement with satellite estimates for the same period. Lateral transports of heat and salt were influenced by an anticyclonic eddy in the survey area, and it is suggested that anticyclonic eddies, which form near the Central American coast, may carry anomalously warm sea surface temperature toward the west and become preferential sites for heavy rainfall.

Citation: Wijesekera, H. W., D. L. Rudnick, C. A. Paulson, S. D. Pierce, W. S. Pegau, J. Mickett, and M. C. Gregg (2005), Upper ocean heat and freshwater budgets in the eastern Pacific warm pool, *J. Geophys. Res.*, *110*, C08004, doi:10.1029/2004JC002511.

1. Introduction

1.1. Eastern Pacific Investigation of Climate Processes in the Coupled Ocean-Atmosphere System (EPIC) Objectives

[2] The Eastern Pacific Investigation of Climate Processes in the Coupled Ocean-Atmosphere System (EPIC2001) was an intensive air-sea interaction process study in the cold-tongue/Inter-Tropical Convergence Zone (ITCZ) complex along 95°W [*Cronin et al.*, 2002; *Raymond et al.*, 2004]. One of the major motivations of EPIC2001 was to examine physical processes that are poorly represented by model parameterizations in atmosphere-ocean coupled models. The program was designed to observe and understand the ocean-atmosphere processes responsible for the structure and evolution of the large-scale atmospheric heating gradients in the equatorial and eastern Pacific portions of the cold-tongue/ITCZ complex including (1) the processes responsible for deep convection in the ITCZ including its variability, strength, and location, (2) the evolution of the vertical structure of the atmospheric boundary layer as surface winds flow northward over the cold tongue and the strong sea surface temperature (SST) gradient of the equatorial front, and (3) the role of surface fluxes and upper ocean processes in determining meridional variability in upper ocean properties along 95°W.

[3] The main oceanographic objective of EPIC2001 (hereinafter referred to as EPIC) was to investigate processes that control temperature, salinity, and thickness of the oceanic mixed layer in the eastern Pacific warm pool (Figure 1). The factors that control SST may include (1) surface buoyancy flux and wind stress, (2) mixing and entrainment at the base of the mixed layer; in particular the effect of energetic but episodic atmospheric forcing events relative to time-mean forcing, and (3) horizontal and vertical advection. Specific questions addressed in this study are (1) can the upper ocean budgets of heat and freshwater be closed to provide independent estimates of

[1]College of Oceanic and Atmospheric Sciences, Oregon State University, Corvallis, Oregon, USA.
[2]Scripps Institution of Oceanography, University of California, San Diego, La Jolla, California, USA.
[3]Kachemak Bay Research Reserve, Homer, Alaska, USA.
[4]Applied Physics Laboratory, University of Washington, Seattle, Washington, USA.

0148-0227/05/2004JC002511$09.00

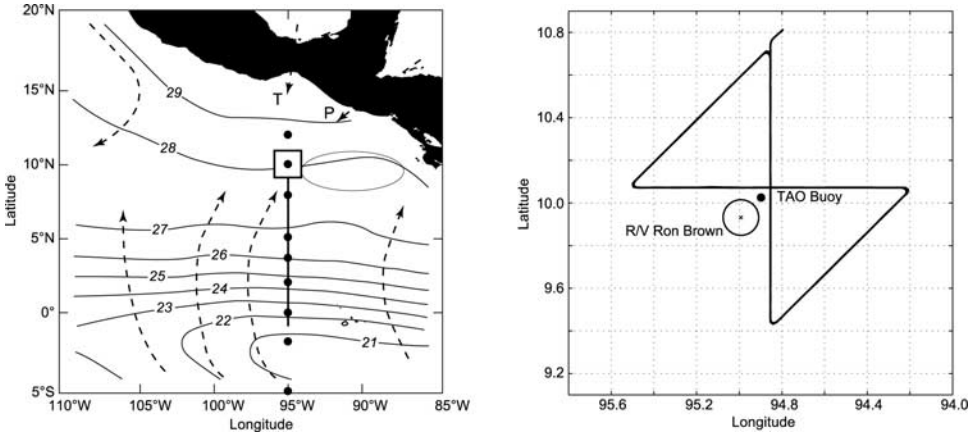

Figure 1. Map of the study region along with the location of the butterfly pattern. (left) Solid circles denote locations of tropical atmosphere ocean (TAO) moorings along 95°W. Contours indicate sea surface temperature (SST) for the month of September from the *Levitus* [1982] climatology. Dashed arrows indicate southerly winds and gap winds over the Isthmus of Tehuantepec (T) and the Gulf of Papagayo (P). The square box shows the intensive study area, where survey ships were located between 13 September and 3 October 2001. The solid line extending to 1°S denotes the equatorial track of R/V *New Horizon*. The open ellipse denotes the climatological center of the Costa Rica dome. (right) An enlarged view of R/V *New Horizon*'s survey (butterfly) pattern with respect to location of the TAO buoy and the stationary ship, R/V *Ron Brown*. The center of the butterfly was located at 10.072°N, 94.854°W. The solid circle shows the position of the TAO buoy (10.026°N, 94.898°W). *Ron Brown* operated in a 10 nm diameter circle with its center (9.932°N, 94.992°W) located 8 nm southwest of the TAO buoy.

net surface heat flux and rainfall?, (2) how important is the effect of horizontal advection on ocean mixed layer temperature and salinity?, and (3) what is the relationship between mesoscale oceanic processes and air-sea fluxes?

[4] In the following, we address these questions by examining upper ocean heat and salinity budgets in the eastern Pacific warm pool for a 19 day R/V *New Horizon* survey made as a part of EPIC (Figure 1). We examine and quantify advective transports and their relation to air-sea interaction. The analysis of heat and freshwater budgets allows evaluation of the relative importance of different upper ocean processes and their effect on the evolution of thermohaline fields and mixed layer depths. Air-sea fluxes over the warm pool under the ITCZ are poorly known and the accuracy of model predictions is uncertain. Independent estimates of heat and freshwater fluxes from oceanic budgets are useful for validating direct and indirect estimates from atmospheric measurements. For example, tropical rainfall is highly intermittent in space and time; therefore the area-averaged rainfall from a freshwater budget is valuable for comparison with rainfall measured by a Doppler radar and optical rain gauges. Together with air-sea fluxes, horizontal currents, and turbulent mixing profiles from a stationary ship, R/V *Ronald H. Brown*, and wind stress, sea surface temperature (SST), sea surface height (SSH) and rainfall rate from satellite observations, the R/V *New Horizon* transects of temperature, salinity and horizontal velocity provide a unique data set to explore thermal and freshwater budgets in the oceanic surface layer.

1.2. Eastern Pacific Warm Pool

[5] The eastern Pacific warm pool, which surrounds the site of the EPIC experiment, is defined by SST greater than 27.5°C to the east of 120°W. The north, south and east boundaries are, respectively, the cooler water of the California Current (~18°N), the equatorial cold tongue (~5°N), and the Central American landmass. The warmest water is found close to the Central American coast during summer and early fall, where SST is about 1°C warmer than at the middle of the pool. The warm pool lies under the ITCZ and the North Equatorial Countercurrent (NECC) flows eastward through the southern portion of the warm pool [e.g., *Kessler*, 2002]. *Xie et al.* [2005] have recently described air-sea interaction over the eastern Pacific warm pool based primarily on satellite observations.

[6] The eastern Pacific warm pool exhibits an annual cycle with cold SST, weak winds, and a minimum in rainfall from February through March, and warm SST, moderate winds, and heavy rainfall from July through September [*Xie et al.*, 2005]. Winds blowing from south of the equator converge with northeasterlies at 6°–9°N into the ITCZ, a zone of active atmospheric convection and heavy rainfall which extends westward across most of the Pacific. There is also seasonal variability in easterly winds through the gaps in the Central American cordillera, namely the Isthmus of Tehuantepec, the Gulf of Papagayo, and the Gulf of Panama. These wind jets have positive wind stress curl on their left flank and negative curl on their right [*Chelton et al.*, 2000; *Kessler*, 2002; *Mitchell et al.*, 1989].

[7] Oceanic circulation in the warm pool is relatively complex due to variable gap winds, which generate upwelling (positive wind stress curl) and downwelling (negative wind stress curl) extending a few hundred kilometers from the Central American coast. Positive wind stress curl associated with the gap winds and southerly flow into the ITCZ generates a persistent, cyclonic feature centered near 9°N,

90°W called the "Costa Rica dome" [e.g., *Fiedler*, 2002; *Kessler*, 2002]. The annual mean extent of the dome, denoted by the 45 m depth contour of the 20°C isotherm, extends from the Central American coast to 96°W in east-west direction and from 6°N to 11°N in the north-south direction [*Fiedler*, 2002, Figure 11]. Cyclonic circulation associated with the dome extends from the Central American coast to more than 100°W in the east-west direction and from 6°N to 11°N in the north-south direction [*Kessler*, 2002]. The EPIC site was located in the northeast sector of the cyclonic cell, where mean geostrophic currents at the surface are westward with a magnitude of about 0.15 m s^{-1}, and mean Ekman flow is toward the northwest at 0.02 m s^{-1} [*Kessler*, 2002, Figures 3 and 4]. *Kessler* [2002] estimated 3.5 Sv of upwelling at the center of the dome and argued that a first-order dynamical description of the northeast tropical Pacific is consistent with the Sverdrup balance.

[8] The EPIC site was in an area where mesoscale eddies are energetic [*Giese et al.*, 1994; *Muller-Karger and Fuentes-Yaco*, 2000; *Fiedler*, 2002]. *Giese et al.* [1994] reported anticyclonic eddies moving westward at a speed of 0.17 m s^{-1} from the coast of Central America. The formation of the eddies is seasonal and their lifetime is up to 6 months. Negative wind stress curl associated with the Papagayo and Tehuantepec wind jets, appears to generate the eddies [*Clarke*, 1988; *McCreary et al.*, 1989]. *Hansen and Maul* [1991] suggest that anticyclonic eddies are also generated by the interaction of NECC with the coast of Central America. The NECC turns northward at the coast, generating anticyclonic vorticity that results in eddy production in late summer and fall when the current is strongest.

[9] Apart from seasonal cycles there is substantial variability in the atmosphere on shorter (days to weeks) timescales. Convection over the warm pool occurs episodically on timescales of a few days, perhaps initiated by the passage of easterly waves [*Serra and Houze*, 2002; *Peterson et al.*, 2003]. The warm pool acts as a generation site for tropical storms, including hurricanes, in the eastern Pacific (see http://www.nhc.noaa.gov).

[10] The outline of this paper is as follows. Data sets used in this study are described in section 2. In section 3, an overview of the observations is presented; heat and salinity balances are described in section 4. The results are discussed and summarized in section 5.

2. Data Acquisition

[11] The R/V *New Horizon* survey focused on the spatial structure of the time-varying thermohaline fields of the upper ocean centered near 10°N, 95°W. The sampling plan was designed to resolve meridional and zonal scales of O(1 km) to O(100 km) and vertical scales of a few meters, and also to complement time series measurements from EPIC-enhanced tropical atmosphere ocean (TAO) moorings and the stationary ship, R/V *Ron Brown* (Figure 1). Measurements from the R/V *Ron Brown* near the center of the survey pattern yielded better temporal resolution near the center of the survey pattern compared to the underway hydrographic survey from the R/V *New Horizon*. The center of the butterfly survey was chosen to be close to the TAO mooring at 10°N, 95°W and the stationary ship R/V *Ron Brown*. The long sections of the butterfly pattern were oriented in meridional and zonal directions to determine mesocale gradients of hydrographic fields. The time required to complete a single butterfly pattern (146 × 146 km) at a speed of 8 knots was approximately 34.5 hours, which is about half the inertial period at 10°N. Hence an average of two consecutive butterfly surveys minimizes the effect of inertial motions on the spatial gradients.

[12] Underway hydrographic data were collected by use of a SeaBird conductivity-temperature-depth (CTD) measuring instrument mounted on an undulating platform, SeaSoar. Horizontal velocity data were obtained from the ship-mounted 150 kHz acoustic Doppler current profiler (ADCP). The butterfly survey (Figure 1b) lasted from 14 September to 3 October 2001, and produced 11 meridional and zonal sections. The sampling rate of the CTD was 24 Hz, and the nominal operating depth range was 0–200 m with a cycling period of about 8 min, which corresponds to a horizontal distance between upcasts of 1.9 km at a mean ship speed of 4 m s^{-1}. In this study we used 1 s and 8 min temporal and 5 m vertical averages of temperature, salinity, and potential density. The nominal depth range of the ADCP was 15–300 m and the vertical resolution was about 8 m. One minute averages of temperature and salinity at a depth of ~0.1 m were obtained by pumping near-surface water through a shipboard (SeaBird) thermosalinograph. Temperature and salinity, and optical properties at a depth of 3 m were also recorded using ship's flow-through system.

[13] Meteorological measurements were recorded at 1 min intervals. Atmospheric measurements included wind speed and direction, humidity, air temperature, incoming shortwave and longwave radiation, rainfall rates, and rain temperature. Both funnel gauges and optical rain gauges (ORGs) measured rainfall at different locations on the ship. Two sets of GPS and navigational information were recorded at 1 Hz resolution. Atmospheric boundary layer fluxes were recorded using a sonic anemometer provided by R. Weller. K. Gage and his colleagues measured rainfall signatures with an S-band radar.

[14] In addition to data from the R/V *New Horizon*, we used time series measurements from the R/V *Ron Brown*. These included horizontal currents from a 150 kHz ADCP, temperature, salinity, and turbulent mixing rates from a modular microstructure profiler (MMP) [*Gregg et al.*, 2002], near-surface temperature at 0.05 m depth and air-sea fluxes of heat and freshwater. Satellite measurements of surface wind from the QuikSCAT scatterometer, sea surface temperature (SST) from the Tropical Rainfall Measuring Mission microwave imager (TMI), and sea surface height (SSH) from a combination of three satellites were used to examine spatial and temporal structure in the region surrounding 10°N, 95°W. We used Version 3 QuikSCAT winds and Version 3a TMI ocean products (data are available at http://www.remss.com). SSH data were from the Pathfinder 9.2 version of TOPEX, ERS, and GFO satellites (data are available at COAS/OSU archives [*Strub and James*, 2000]).

3. Overview of the Observations

[15] In this section, we present an overview of data collected during the R/V *New Horizon* butterfly surveys

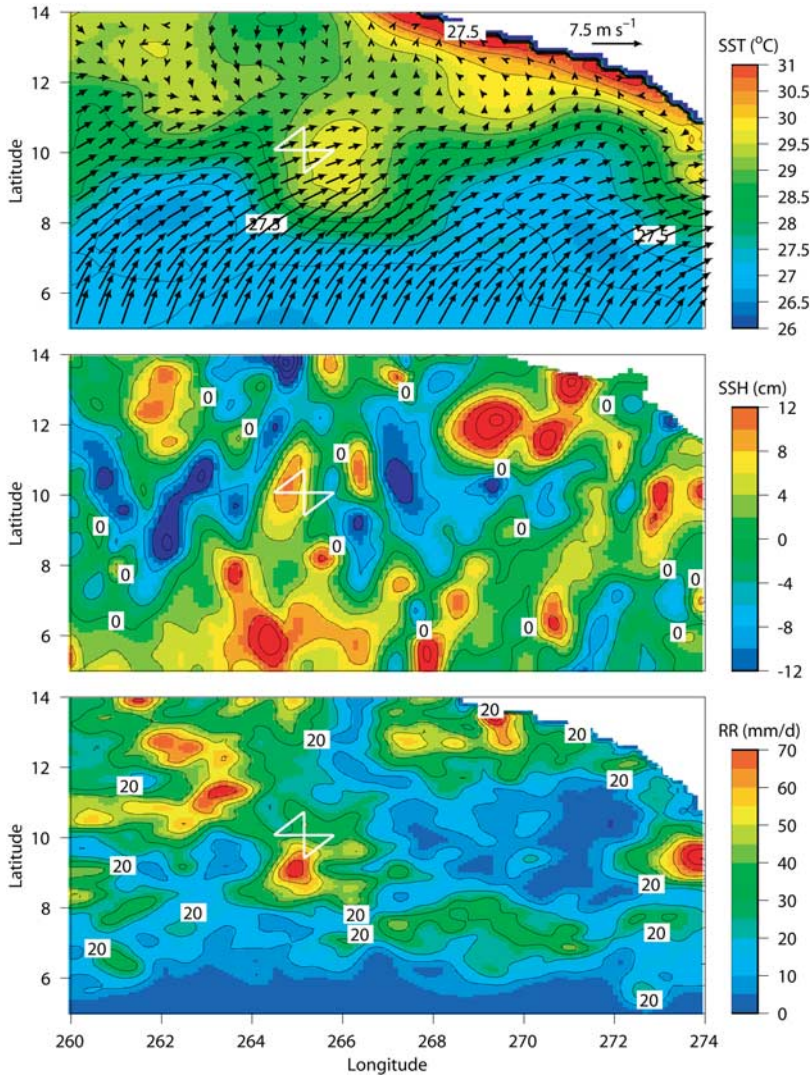

Figure 2. (top) Cruise-averaged map of SST (color contours) from the Tropical Rainfall Measuring Mission microwave imager (TMI) and wind vectors (arrows) derived from QuikSCAT. The contour interval of SST is 0.5°C. (middle) Cruise-averaged sea surface height (SSH) anomaly estimated from Pathfinder 9.2 TOPEX, Pathfinder 9.2 ERS-2, and Pathfinder 9.2 GFO satellite data sets. (bottom) TRMM TMI derived rain rates. The butterfly pattern is marked in white. TMI and QuikSCAT data sets can be found at http://www.remss.com. Analysis of SSH data is described by *Strub and James* [2000].

centered at 10.072°N, 94.854°W (nominally 10°N, 95°W) before discussing the analysis of heat and freshwater budgets in subsequent sections. Complementary simultaneous observations from satellites and from the R/V *Ron Brown* are also summarized.

[16] Cruise-averaged sea surface temperature fields from satellite measurements show meandering temperature contours with an eddy-like surface signature in the vicinity of the observational site (Figure 2 (top)). We used 3 day averaged, 25 km spatially interpolated TMI SST and QuikSCAT wind stress to obtain the cruise-averaged temperature and wind patterns over the warm pool (Figure 2). The spatial resolution of 3 day averaged TMI SST used in this study was about 50 km. Winds from the south weakened toward the north and veered to the east over the warm pool, consistent with surface convergence associated with the ITCZ. The TMI temperature record showed a warm water anomaly with SST ~29.7°C to the east of 10°N, 95°W, and a similar spatial-scale cold water anomaly with SST ~26.8°C to the southeast of EPIC site. The mesoscale zonal temperature gradient at 10°N, 95°W was larger than the meridional temperature gradient (Figure 2).

[17] Combined observations of sea surface height (SSH) from three satellites confirm the presence of an anticyclonic eddy in the vicinity of 10°N, 95°W during the observational period (Figure 2 (middle)). The altimeter data indicates that the eddy had a positive SSH anomaly of 6–12 cm with diameter of about 200 km. Examination of a sequence of SSH images (not shown) indicates that the eddy propagated toward the west at a speed of about 0.15 m s^{-1}. The westward movement and the anticyclonic circulation of the eddy are qualitatively consistent with the observed ADCP measurements and the estimated geostrophic currents from SeaSoar hydrographic fields (see section 4.3.2).

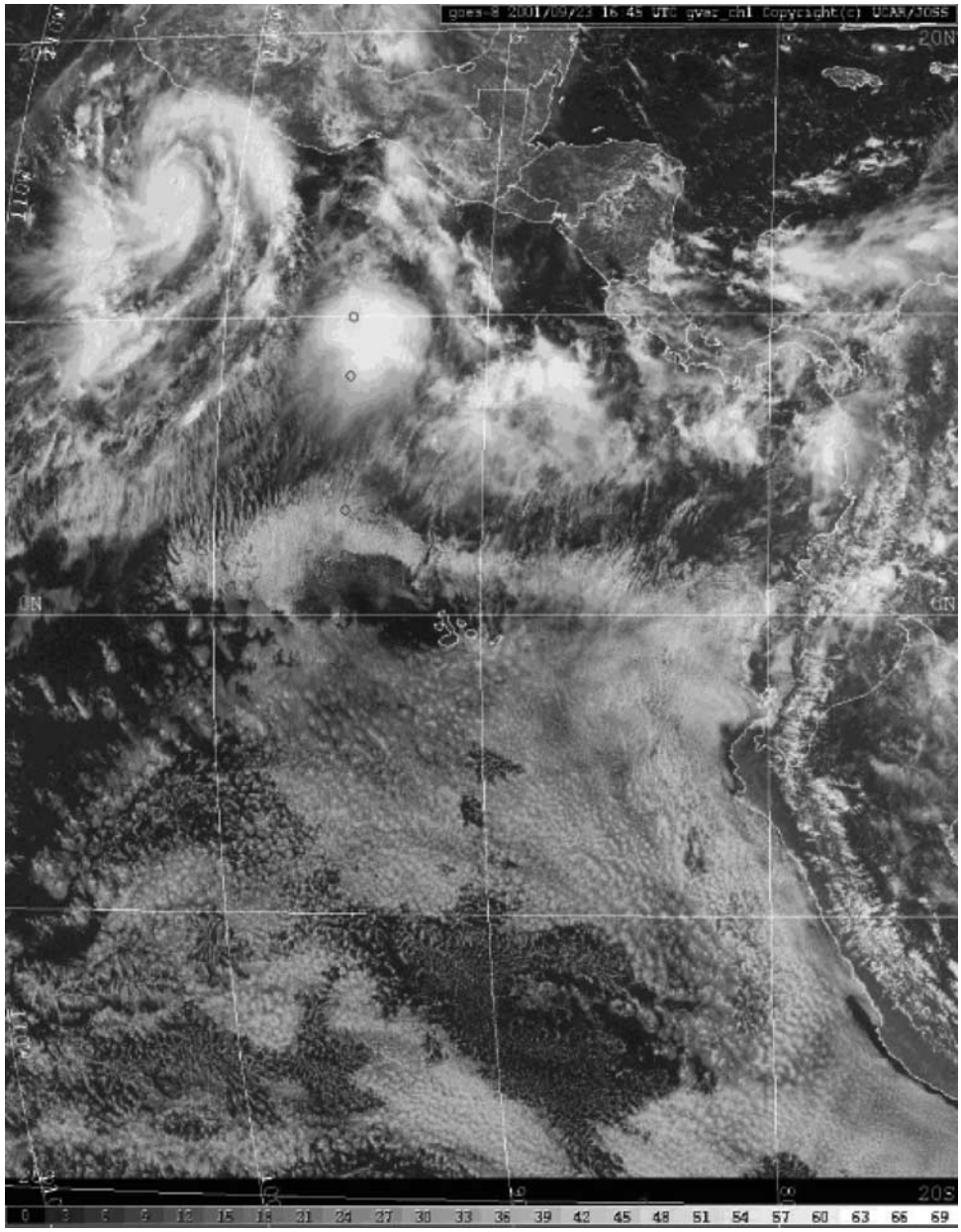

Figure 3. GOES-8 satellite channel 1 imagery at year day = 266.6979 (23 September, 1645 UTC). Hurricane Juliette can be seen in the northwest corner of the image, and a deep convective system centered near 10°N, 95°W is directly above the survey area (http://www.joss.ucar.edu/epic/dm/data_access_frame.html).

The eddy was also mapped by *Shay et al.* [2002] from measurements made with expendable current profilers and expendable CTD instruments dropped from aircraft as part of the EPIC experiment.

[18] Rainfall rate estimated from satellite passive microwave observations and averaged over the warm pool for the cruise was highly variable (Figure 2 (bottom)). The maximum located near the butterfly pattern exceeds 70 mm d^{-1}, while regions less than 150 km away had mean rainfall rates of less than 10 mm d^{-1}. The high rainfall rates northwest of the butterfly pattern were at least partly due to the passage of a tropical cyclone (Juliette) past that location. Rainfall over the Costa Rica dome centered at 9°N, 90°W was lower than north, south, and west of the dome, which is consistent with annual climatology.

[19] During our surveys the warm pool was subjected to weak to moderate winds along with periods of heavy rainfall associated with deep convection (Figures 2–4). Winds from the west were weak at the beginning, and became moderately strong after day 266 (23 September 2001 (Figure 4)). Periods of moderate wind stress ($\sim$0.15 N m^{-2}) lasting for several hours coincident with heavy rainfall (1 min averages up to 100 mm h^{-1}) were observed on days 266 and 267, when the butterfly pattern was under a deep convective system (Figure 3). Heavy cloud cover associated with deep convection blocked solar radiation, which contributed to cooling the

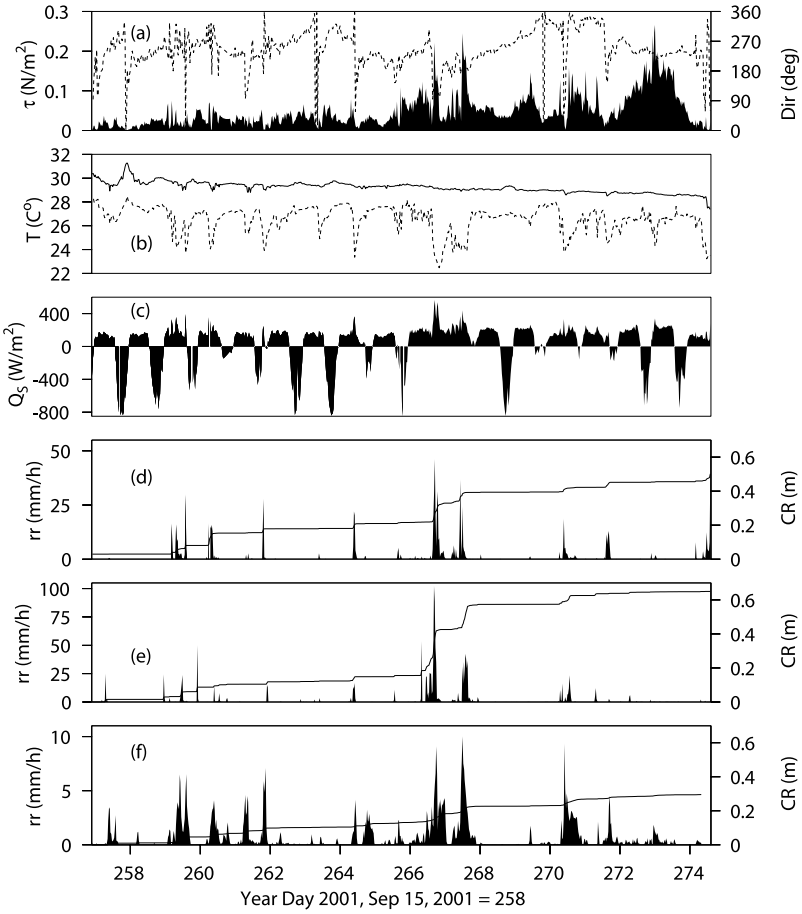

Figure 4. Time series plots of 30 min averaged meteorological data. (a) Wind stress (N m^{-2}) and direction (dashed line) at 18.5 m above the sea surface from R/V *Ron Brown*. (b) Sea surface temperature at 0.05 m below the sea surface and air temperature at 15.5 m above the sea surface from *Ron Brown*. (c) Net surface heat flux (W m^{-2}) from R/V *Ron Brown*, where Q_S is positive upward. (d) Rainfall rate, *rr* (mm h^{-1}), and cumulative rain, *CR* (m), from R/V *Ron Brown*'s optical rain gauge (ORG). (e) Rainfall rate and cumulative rain from R/V *New Horizon*'s ORG. (f) Rain rate and its accumulation from C-band Doppler radar. Radar rainfall data has been averaged in a circle of radius 10 km around R/V *Ron Brown*.

sea surface (Figures 3 and 4). The cruise-averaged net surface heat flux was 30 W m^{-2} of cooling (J. Hare et al., A seven-cruise sample of clouds, radiation, and surface forcing in the equatorial eastern Pacific, submitted to *Journal of Climate*, 2005, hereinafter referred to as Hare et al., submitted manuscript, 2005), which may be compared to a climatological value of 28 W m^{-2} of heating for the month of September [*da Silva et al.*, 1994]. The reduction of SST measured on the *Ron Brown* at a depth of 0.05 m was 1.3°C based on a linear least squares fit. The atmospheric boundary layer over the warm pool was unstable, since SST was always warmer than air temperature (T_{air}) at 15.5 m above the sea surface; on average, SST – T_{air} was 2.6°C. Like SST, T_{air} also decreased with time, but air temperature exhibited short-timescale fluctuations at quasi-regular intervals. On many occasions a rapid drop in air temperature was accompanied by a sudden change in wind direction and rainfall, suggesting downward movement of cold air associated with atmospheric convection.

[20] Cumulative rainfall during the field experiment from ORGs ranged from 0.5 m (*Ron Brown*) to 0.6 m (*New Horizon*), which was a factor of two larger than the 0.3 m estimated from the Doppler radar measurements (Figure 4). The Doppler radar mounted on R/V *Ron Brown* produced rainfall maps at 1 km height averaged over 2 km square pixels and 10 min intervals (http://www.joss.ucar.edu/epic). The ORGs made measurements of rainfall averaged over a 30 cm path and 1 min intervals. Rainfall was largest on days 266 and 267, and the accumulation of rainfall for those 2 days observed on the R/V *New Horizon* accounted for nearly two-thirds of the total (Figure 4).

[21] Cruise-mean profiles of temperature (*T*), salinity (*S*), and potential density anomaly (σ_θ) showed a weakly stratified layer in the upper 20 m atop a strongly stratified pycnocline (Figures 5a–5e). The largest mean vertical temperature gradient (about 0.4°C m^{-1}) was near 40 m, whereas the largest vertical salinity gradient of (about −0.04 psu m^{-1}) was near 30 m (Figures 5d–5e). The differences in depths of the largest vertical gradients of T and S may be due to the different sources for heat and freshwater. Rainfall penetrates the surface to only a minor extent, but solar radiation penetrates significantly, which is qualitatively consistent with the difference in depths of the maximum vertical *T* and *S* gradients. The near-surface

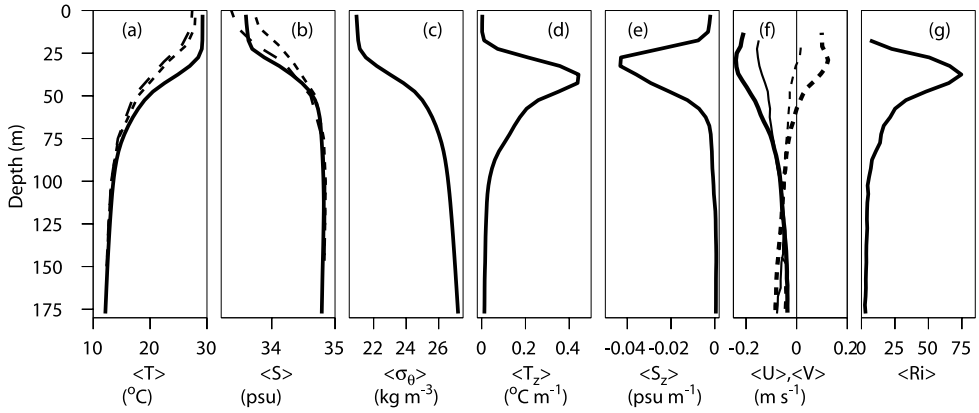

Figure 5. Cruise-averaged hydrographic and velocity profiles: (a) temperature T along with the *Levitus* [1982] climatology for summer (long dashed line) and for fall (short dashed line), (b) salinity S along with the *Levitus* [1982] climatology for summer (long dashed line) and for fall (short dashed line), (c) potential density anomaly σ_θ, (d) vertical temperature gradient T_z, and (e) vertical salinity gradient S_z from SeaSoar conductivity-temperature-depth (CTD). (f) Zonal velocity (solid line) and meridional velocity (dashed lines) from the 150 kHz acoustic Doppler current profilers (ADCPs) of R/V *New Horizon* (thin lines) and R/V *Ron Brown* (thick lines). (g) Richardson Number (Ri) estimated from *New Horizon* velocity and density measurements. Data for a given butterfly section were averaged into 5 vertical m intervals in depth and 8 min in time (or 1.9 km spatially) before averaging over the butterfly path.

stratification was weaker than long-term climatology from *Levitus* [1982] (Figures 5a and 5b), but there is excellent agreement of both temperature and salinity with the *Levitus* [1982] atlas below 75 m. The observed near-surface temperature during EPIC was warmer than *Levitus* [1982] climatology, and surface salinity was intermediate between summer and fall *Levitus* [1982] climatology. The difference in the near-surface shapes of the EPIC temperature and salinity profiles compared to *Levitus* [1982] was consistent with more active near-surface mixing during EPIC than long-term climatology, which was in turn, consistent with more highly energetic storms than average and with surface cooling rather than heating. Energetic storms are consistent with higher than average cloud cover, a reduction of solar insulation below average, and with SSTs lower than average (Figure 5a).

[22] The near-inertial wave band had the highest energy in the spectrum of horizontal velocity in the weakly stratified surface layer (Figure 6). Spectral estimates at a depth of 17 m show a well-defined inertial peak with an rms value of 0.25 m s^{-1} and a semidiurnal peak with an rms value of 0.08 m s^{-1}. The high-frequency end of the spectrum shows an approximate slope of -1. Frequency spectra of horizontal velocity were computed from 5 min averaged ADCP records from R/V *Ron Brown*. Spectral levels of the zonal and meridional velocity components were similar. We also noted that vertical shear of horizontal currents in the thermocline was strong in the near-inertial band. During the Coupled Ocean Atmosphere Response Experiment (COARE), semidiurnal tides dominated in the spectrum of horizontal velocity in the western equatorial Pacific Ocean warm pool near 1.8°S, 156°E [*Feng et al.*, 1998a], where the inertial period is about 15.9 days. *Feng et al.* reported that barotropic and baroclinic semidiurnal tides accounted for 40–60% of the observed semidiurnal band velocity variance. *Feng et al.* [1998a] adapted a spatial interpolation technique described by *Candela et al.* [1992] to decompose barotropic and baroclinic components of the semidiurnal tide. Such an analysis is not appropriate in the present study because the major temporal variability observed during EPIC was in the inertial wave band, which was highly baroclinic.

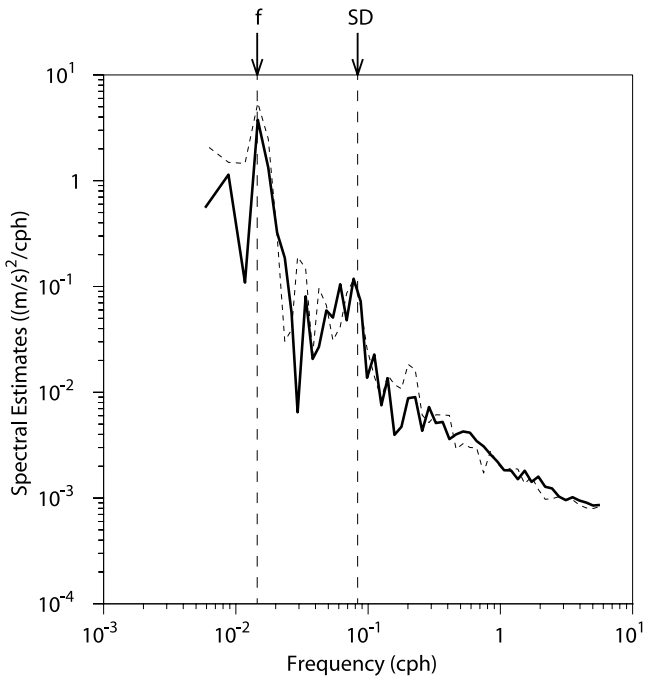

Figure 6. Spectra of the R/V *Ron Brown* ADCP velocity components at a depth of 17 m. The solid line denotes the zonal component, and the dashed line denotes the meridional component.

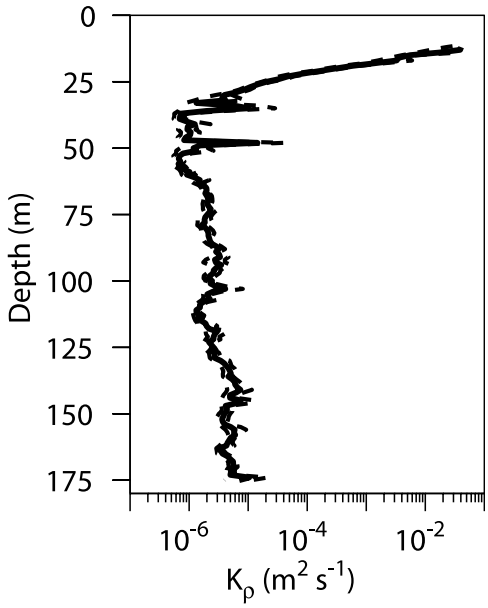

Figure 7. Cruise-mean eddy diffusivity profile (equation (1)) based on modular microstructure profiler (MMP) data [from *Gregg et al.*, 2002]. Dashed lines denote 95% confidence based on the bootstrap method.

[23] Low-frequency currents were estimated from ship ADCP records by filtering near-inertial and higher-frequency motions by use of a low-pass (69 hour) running mean filter. It is likely that ADCP records from the *New Horizon* contained inertial oscillations that varied in both time and space because the ship moved around a butterfly pattern; therefore our filtering techniques may not have completely removed near-inertial motions from the *New Horizon* record. Hence we also use velocity records from the stationary ship, R/V *Ron Brown*. The "box car" filter reduced the inertial peak in *Ron Brown* velocity data (Figure 6) by at least a factor of 400. The cruise averaged ADCP profiles show that mean surface currents were toward the west-northwest (*Ron Brown*) or west (*New Horizon*) in the upper 50 m (Figure 5f). Mean currents were weak below 100 m. Westward flow of 0.15 m s^{-1} (*New Horizon*) to 0.25 m s^{-1} (*Ron Brown*) in the upper 25 m is qualitatively consistent with annual mean westward surface geostrophic velocity of 0.1 m s^{-1} at 10°N, 95°W associated with the Costa Rica Dome [*Kessler*, 2002].

[24] The vertical shear of horizontal velocity was largest at near-inertial frequencies [*Gregg et al.*, 2002], but the total shear squared was not large enough to cause the mean Richardson Number (*Ri*) to fall below the critical value of 0.25 to intensify shear-driven mixing in the weakly stratified near surface layer (Figure 5g). Even though cruise-mean values of *Ri* were well above the critical value, instantaneous or short-term averages may have been less. The cruise-averaged *Ri* was about 5 at 20 m and increased to about 70 at 38 m, where buoyancy frequency was a maximum (Figures 5d, 5e, and 5g). Buoyancy frequency and squared shear of horizontal velocity were estimated, respectively, from 5 m vertical and 8 min averaged SeaSoar CTD and R/V *New Horizon* ADCP profiles. Large values of mean *Ri* ($\gg$1) in the pycnocline were consistent with weak turbulent mixing reported by *Gregg et al.* [2002; see also *Raymond et al.*, 2004], who found that eddy diffusivity decreased exponentially as a function of depth between 20 m and 40 m (Figure 7).

[25] The mean eddy diffusivity for mass, heat and salt transfer [*Osborn*, 1980],

$$K_\rho = K_T = K_S = \frac{0.2\langle \varepsilon \rangle}{\langle N^2 \rangle}, \quad (1)$$

was obtained from MMP data described by *Gregg et al.* [2002], where ε is the turbulent kinetic energy (TKE) dissipation rate, and N is the buoyancy frequency. The angle bracket denotes the cruise average. K_ρ was 2×10^{-4} m^2 s^{-1} at 20 m and decreased to about 2×10^{-6} m^2 s^{-1} at 40 m, where stratification was strongest and *Ri* was largest (Figure 5f). The uncertainty in K_ρ is mainly due to the intermittency of ε. The 95% confidence levels of K_ρ shown in Figure 7 were obtained by use of the bootstrap method [*Efron and Gong*, 1993].

[26] Mixed layer depth (MLD) was computed from density profiles measured by SeaSoar (*New Horizon*) and MMP (*Ron Brown*) (Table 1). The computation of MLD was based on the depth at which the density exceeds the surface density by a specified step ranging from 0.01 to 1.0 kg m^{-3} (Table 1). The SeaSoar density data was averaged over 1 s intervals and then over 1 m vertical intervals prior to computation of MLD. The MMP density data were averaged over 1 m vertical intervals. Measurements of density from SeaSoar are along a glide path at an angle of about 15° from the horizontal. Hence horizontal variations of density may be interpreted as vertical variations and the computation of MLD from SeaSoar measurements was biased low, particularly when the density difference was small. The MMP profiles were measured near the stern of the ship where the surface layer may have been mixed by turbulence in the ship's wake. Hence estimates of MLD from the MMP data may have been biased high. The statistics of MLD in Table 1 are quite different for SeaSoar and MMP with a density step of 0.01 kg m^{-3}, but the difference decreases

Table 1. Cruise-Averaged Mixed Layer Depths Along With Standard Deviation (Std), Maximum (Max), and Minimum (Min) for Different Density Steps[a]

	Layer Thickness *h*, m			
Density Step $\Delta\sigma_\theta$, kg m^{-3}	Mean	Std	Max	Min
SeaSoar Profiles				
0.01	6	2	14	0.4
0.05	12	4	32	0.5
0.1	19	6	32	0.6
0.5	27	4	39	3.3
1.0	30	3	41	15
MMP Profiles				
0.01	12	7.7	28	1
0.05	15	7.4	30	1
0.1	20	6.0	31	1
0.5	25	3.7	34	3
1.0	28	3.8	39	3

[a] $\Delta\sigma_\theta = \sigma_\theta(h) - \sigma_\theta(z_{min})$; $\sigma_\theta(z_{min})$ is the density at the shallowest depth, and $\rho(h)$ is the density at the layer depth *h*. SeaSoar estimates were based on 1 s and 1 vertical m averaged profiles, and MMP estimates were based on 1 vertical m averaged profiles.

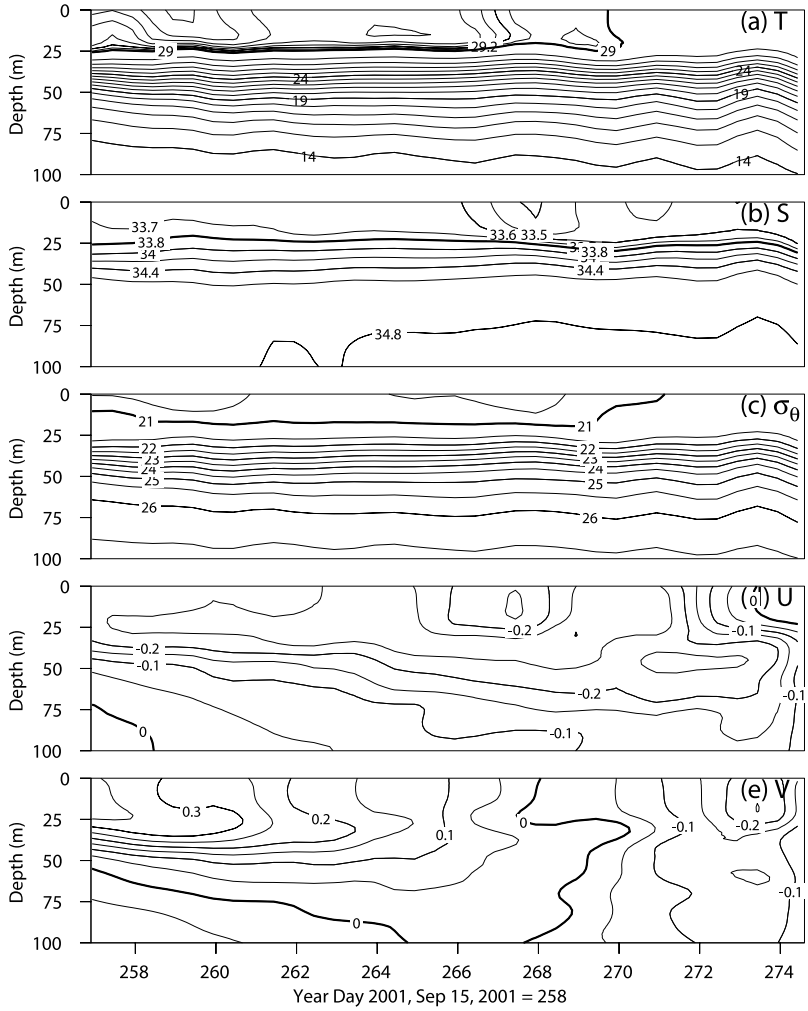

Figure 8. Time-depth (t, z) fields of T, S, and σ_θ from SeaSoar and U and V from the R/V *Ron Brown* ADCP. ADCP data were first smoothed with a 2.87 day running mean filter to remove the inertial wave signal. (a) Temperature: for $T \geq 29°C$, $\Delta T = 0.1°C$, and for $T < 29°C$, $\Delta T = 1°C$. (b) Salinity: for $S \leq 33.8$, $\Delta S = 0.1$ psu, and for S > 33.8 psu, $\Delta S = 0.2$ psu. (c) Potential density anomaly: for $\sigma_\theta \geq 21$ kg m^{-3}, $\Delta\sigma_\theta = 0.5$ kg m^{-3}, and for $\sigma_\theta < 21$ kg m^{-3}, $\Delta\sigma_\theta = 0.1$ kg m^{-3}. (d) Zonal velocity: $\Delta U = 0.05$ m s^{-1}. (e) Meridional velocity: $\Delta V = 0.05$ m s^{-1}.

rapidly as the step size increases. It has been reported by several researchers [e.g., *Smyth et al.*, 1996; *Wijesekera and Gregg*, 1996] that the MLD defined with a density step of 0.01 kg m^{-3} coincides with the depth of a mixed layer with high TKE dissipation, i.e., a mixed layer that is actively mixing. The MLD statistics computed from the MMP measurements for a density step of 0.01 kg m^{-3} are likely to be more accurate that the corresponding statistics from SeaSoar (Table 1). One may conclude that the average depth of the actively mixing layer was no greater than 12 m and the maximum depth of this layer did not exceed 28 m.

[27] Much of the temporal variability in oceanic temperature (T) and salinity (S) was limited to the weakly stratified near-surface layer, where diurnal heating and rainfall played a significant role in producing anomalies of T and S. The effect of diurnal heating on near-surface temperature was most significant during the first 2 days of the experiment when winds were light and solar insulation was strong (Figure 4).

[28] Low-salinity and low-temperature anomalies in the upper ocean were caused by heavy rainfall (Figures 4, 8, and 9). Low-salinity surface anomalies have high stratification at their base which limits mixing and entrainment (Figures 8 and 9). The temporal variability of T and S was relatively small below the main pycnocline. The time-depth series of hydrographic fields (Figures 8 and 9) was constructed by averaging north to south and east to west segments along the butterfly path (Figure 1). Zonal velocity (U) in the upper 100 m was mostly westward, while meridional velocity (V) was northward at the beginning and then switched toward the south 6 days before the end of the experiment. The change in meridional velocity was consistent with westward movement of an anticyclonic eddy (Figures 2 and 8).

[29] Density stratification was strongest between 20 and 60 m, where buoyancy frequency was as large as 25 cph. Salinity stratification at a depth of 30 m increased by 0.02 psu m^{-1} after day 266, which coincided with freshening

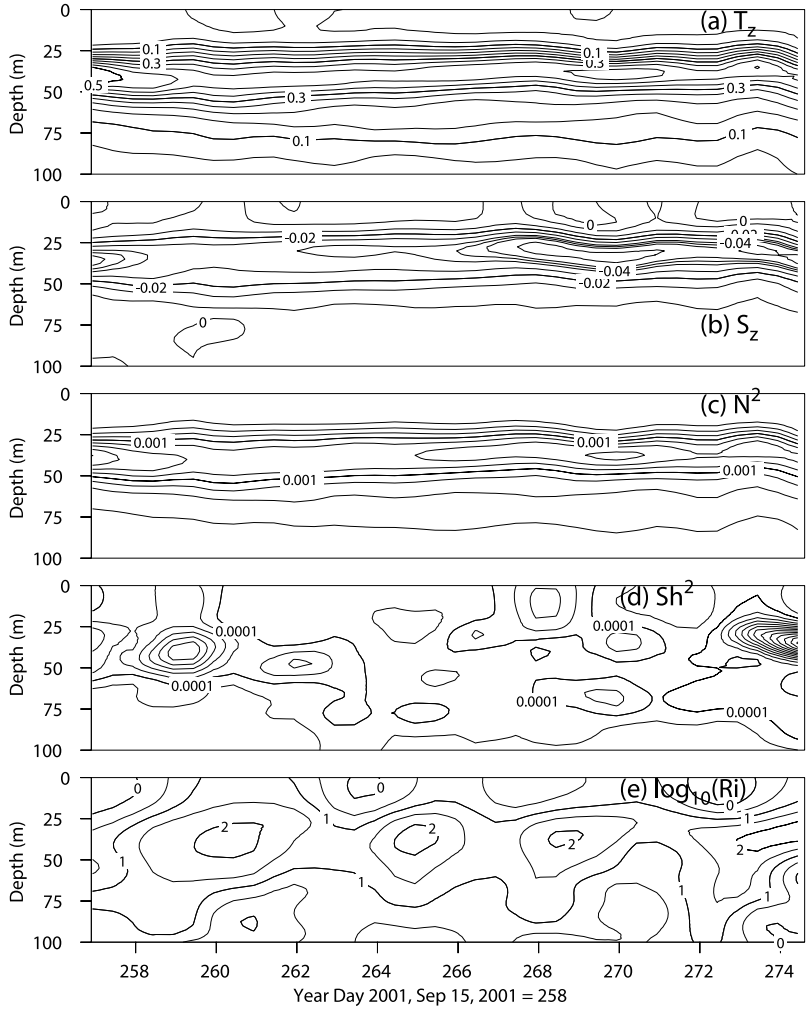

Figure 9. Time-depth (t, z) fields of T_z and S_z, buoyancy frequency squared (N^2), shear squared (shear^2), and Richardson number (Ri). Shear squared $(\partial U/\partial z)^2 + (\partial V/\partial z)^2$ was based on 10 dbar and 8 min averaged velocity fields from R/V *New Horizon*'s ADCP. (a) Vertical temperature gradient, with $\Delta T_z = 5 \times 10^{-2}$ °C m^{-1}. (b) Vertical salinity gradient, with $\Delta S_z = 0.8 \times 10^{-2}$ psu m^{-1}. (c) Buoyancy frequency squared, with $\Delta N^2 = 2.5 \times 10^{-4}$ s^{-2}. (d) Shear squared, with $\Delta sh^2 = 5 \times 10^{-5}$ s^{-2}. (e) $\log_{10}$[Richardson number], with $\Delta[\log_{10}(Ri)] = 0.5$.

of the surface layer due to heavy rainfall (Figure 4). Shear variance was a factor of 5 smaller than the squared buoyancy frequency, and transect-averaged Ri in the upper ocean was significantly greater than 0.25. The magnitude of vertical velocity shear at 35 m depth was higher during the second half of the experiment when the wind stress (and the inertial wave amplitude) was relatively high and variable (Figures 4 and 9). Vertical shear of horizontal velocity was more variable than buoyancy frequency. The modulation of Ri with time (Figure 9), reflects the potential effects of near-inertial waves on mixing in the pycnocline, although eddy diffusivities were small $\sim 10^{-6}$–10^{-5} m^2 s^{-1} (Figure 7).

4. Heat and Salt Budgets

[30] As a step toward understanding basic processes responsible for coupling the ocean and atmosphere in the eastern Pacific warm pool, we investigate heat and fresh water budgets in the weakly stratified layer above the strongly stratified pycnocline. Our objective is to evaluate components of the heat and salt budgets from upper ocean measurements and to compare residual air-sea fluxes of heat and water with independent atmospheric measurements.

4.1. Governing Equations

[31] Vertically integrating the conservation equations for heat and salt from a fixed depth h to the sea surface, we obtain [e.g., *Feng et al.*, 2000]

$$Q_s = -\int_{-h}^{0} \rho_0 c_p \frac{\partial T}{\partial t} dz + F_T(-h) - \int_{-h}^{0} \rho_0 c_p \cdot \left(U \frac{\partial T}{\partial x} + V \frac{\partial T}{\partial y} + W \frac{\partial T}{\partial z} \right) dz + R_S(-h) \quad (2)$$

$$P - E = -\frac{1}{S_o} \int_{-h}^{0} \frac{\partial S}{\partial t} dz + \frac{F_S(-h)}{S_o} - \frac{1}{S_o} \int_{-h}^{0} \cdot \left(U \frac{\partial S}{\partial x} + V \frac{\partial S}{\partial y} + W \frac{\partial S}{\partial z} \right) dz, \quad (3)$$

where $z = 0$ is the surface; h is the depth of the lower boundary; x is positive eastward, y is positive northward and z is positive upward; u, v, and w are zonal, meridional, and vertical velocities, respectively; c_p (= 4000 J kg^{-1} K^{-1}) is the specific heat of seawater at constant pressure and ρ_0 is the mean water density. Note that all upward fluxes are positive. The left hand sides (LHS) of equations (2) and (3) represent surface fluxes, which will be evaluated from oceanic processes represented on the right hand sides (RHS); the first two terms on the RHS represent temporal rate of change and vertical turbulent transport, and the third term represents three-dimensional advection. All the terms in equations (2) and (3) will be cruise averages. The net surface heat flux Q_S (equation (2)) in the atmosphere is given by

$$Q_S = R_S(0) + F_T(0), \tag{4}$$

where $R_S(0)$ is the net surface shortwave radiative flux, and $F_T(0)$ includes net longwave radiative flux, sensible heat flux, and latent heat flux [*Fairall et al.*, 1996]. $R_S(-h)$ is the shortwave radiative flux at depth h, S_0 is the sea surface salinity, and P and E are the precipitation rate and evaporation rate, respectively.

[32] The cruise-averaged vertical fluxes of heat (F_T) and salt (F_S) at a depth h are given by

$$F_T(-h) = -\rho c_p K_T \left\langle \frac{\partial T}{\partial z} \right\rangle \tag{5}$$

$$F_S(-h) = -K_S \left\langle \frac{\partial S}{\partial z} \right\rangle, \tag{6}$$

where K_T and K_S are the mean vertical turbulent diffusivities of heat and salt respectively, and the angle bracket denotes a cruise average. We evaluated cruise-averaged turbulent fluxes from the mean eddy diffusivity profile given in Figure 7 [*Gregg et al.*, 2002; *Raymond et al.*, 2004], which was based on the mean dissipation rate of TKE $\langle \varepsilon \rangle$ divided by the mean density gradient (equation (1)). The mean vertical gradient of T is roughly proportional to the mean vertical gradient of density (Figure 5) or, equivalently, to N^2, which appears in the denominator of the expression for K_T (equation (1)). Therefore the cruise-averaged $F_T(-h)$ is approximately proportional to the cruise-averaged dissipation rate and we may use equation (5) to obtain cruise averages.

[33] The rationale applied to estimating the turbulent flux of heat at depth h may not apply to the turbulent flux of salt because density was determined primarily by temperature, not salinity. The contribution of salinity to the mean vertical density gradient in the depth range from 25 to 50 m was about 25% (Figure 5). In the absence of rainfall, when variations in the vertical density gradient in the upper pycnocline were caused primarily by entrainment, one would expect that vertical gradients of T, S, and density would all be highly correlated and the cruise-averaged turbulent flux of salt would be proportional to the average dissipation rate and equation (6), together with equation (1), could be used to obtain cruise-averaged estimates of $F_S(-h)$. If variations in the vertical gradient of S near the base of the mixed layer were caused by rainfall, the situation is more complex because rainfall is cold compared to the temperature of the ambient surface water and an increase in the magnitude of the vertical gradient of S would be associated with a decrease in the vertical gradient of T. If there is zero correlation between N^2 and the vertical gradient of S, and the dissipation rate is negatively correlated with N^2, then equation (6) in combination with equation (1) would yield underestimates of cruise-averaged turbulent salt fluxes. Therefore cruise-averaged estimates of salt flux obtained with equations (6) and (1) were expected to be lower bounds.

[34] *Ohlmann* [2003] measured penetrative solar radiation profiles during EPIC, and suggested a single exponential curve for penetrative solar radiation $R_S(z)$ for depths below 10 m:

$$R_S(z) = R_S(0)[0.525 \exp(-|z|/13)], \tag{7}$$

where $R_S(0)$ is the net shortwave radiative flux at the surface. Transmissometer measurements of surface water aboard the *New Horizon* during EPIC were consistent with Jerlov Type-1B water, which has a solar flux profile approximated by [*Paulson and Simpson*, 1970]

$$R_S(z) = R_S(0)[0.67 \exp(-|z|) + 0.33 \exp(-|z|/17)]. \tag{8}$$

Ohlmann's [2003] profile gave higher values of penetrative solar flux above 27 m, and lower values of flux below 27 m compared to equation (8) (Figure 10). *Ohlmann*'s [2003] estimate decreased rapidly with depth compared to the estimate based on Jerlov Type-1B water, but the difference between the two formulations was within 10% for the 20–35 m depth range. We used both equations (7) and (8) to compute the penetrative shortwave flux from observations of downward solar radiation on the *Ron Brown* and an albedo of 0.06 [*Payne*, 1972]. As discussed below, uncertainties in $R_S(-h)$ were negligible compared to uncertainties associated with the advection of heat.

[35] For simplicity, heat and freshwater budgets were estimated for a surface layer of constant thickness. In the analysis discussed below, the lower boundary, $z = -h$, was chosen to be well below the mean MLD for a density step of 0.01 kg m^{-3} (Table 1) to minimize the dependence of the calculation on turbulent fluxes of heat and salt at the base of the layer; h was chosen to be well above the level of maximum stratification in the pycnocline to minimize the effects of large and variable advection of heat and freshwater on the budgets. The rationale for selecting layer depths is amplified below.

4.2. Time Rate of Change

[36] The time rate of change of heat content ($-\int \rho C_p \partial T/\partial t dz$) (equation (2)) and salt content ($-1/S_0 \int \partial S/\partial t dz$) (equation (3)) were computed by first evaluating $\partial T/\partial t$ and $\partial S/\partial t$ as a function of depth and then integrating vertically from h to the surface. $\partial T/\partial t$ and $\partial S/\partial t$ were estimated from several different data sets, including T and S from SeaSoar and MMP, other in situ SST and SSS measurements, and SST from TMI satellite observations. As mentioned above, the SeaSoar and near-surface observations from *New Horizon* contain both spatial and tem-

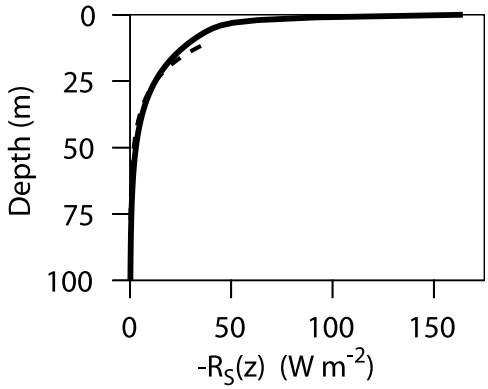

Figure 10. Cruise-averaged penetrative solar radiation for type 1-B water (solid line, equation (7)) and fit to the observed radiation profile from *Ohlmann* [2003] (dashed line, equation (8)).

poral variations around the butterfly, while the MMP observations from *Ron Brown* yielded time series near the center of the butterfly.

[37] The time derivatives (tendencies) were estimated by fitting a straight line through a given time series at each depth. To evaluate trends in T and S from SeaSoar CTD measurements, we treated the SeaSoar hydrographic data for a given depth along the butterfly as a time series. Shown in Figure 11 (left two panels) are time series plots of T and S at 0.1 m from the surface-pumped thermosalinograph system, T and S at 17.5 m from SeaSoar, and T and S at 17 m from MMP, along with least square linear fits to the data (dashed lines). The slope of the least square fit was taken as the cruise-mean time derivative for a given depth. Near-surface temperature tendencies from ship and satellite data were in good agreement with the upper 5 m temperature tendencies from SeaSoar and MMP (Figures 11 and 12). Temperature trends from MMP and SeaSoar agree very well in the upper 25 m, but deviate substantially in the stratified layer below 25 m. The differences between *New Horizon* and *Ron Brown* estimates of $\partial T/\partial t$ below 25 m depth (Figure 12) may be the result of large spatial and temporal variations of temperature in the thermocline, which were sampled in different ways by the two ships; i.e., *Ron Brown* was stationary and *New Horizon* sampled around the butterfly pattern. SeaSoar measures a horizontally averaged time derivative, which may differ from the time derivative at the center of the butterfly even if the SeaSoar sections were densely sampled in both time and space.

[38] Although tendencies of salinity from the two ships are very close between 15 m and 35 m (Figure 12), estimates near the surface tend to depart, perhaps due to the high degree of spatial and temporal patchiness in rainfall (Figure 4), which caused spatially and temporal patchiness in salinity near the surface. The salinity tendency computed from the *New Horizon* data may be more representative of the true tendency averaged over the butterfly because the SeaSoar samples in both space and time and therefore includes many more rain-caused anomalies than the measurements from the *Ron Brown* (Figure 11) (SeaSoar S at 17.5 m and MMP S at 17 m). In the following budget calculations, salinity tendencies from both SeaSoar and MMP were used, but with the MMP value at 17.5 m depth extended without change to the surface to force approximate agreement with the tendency measured at 0.1 m depth on *New Horizon* (Figure 12).

[39] The MMP and SeaSoar observations indicated that the near-surface of the warm pool ocean cooled at a mean rate of 0.062 and 0.071°C d^{-1}, respectively. The difference is small and can be ascribed to differences in sampling. These cooling rates are in excellent agreement with 0.067°C d^{-1}, estimated from TMI measurements of SST at the center

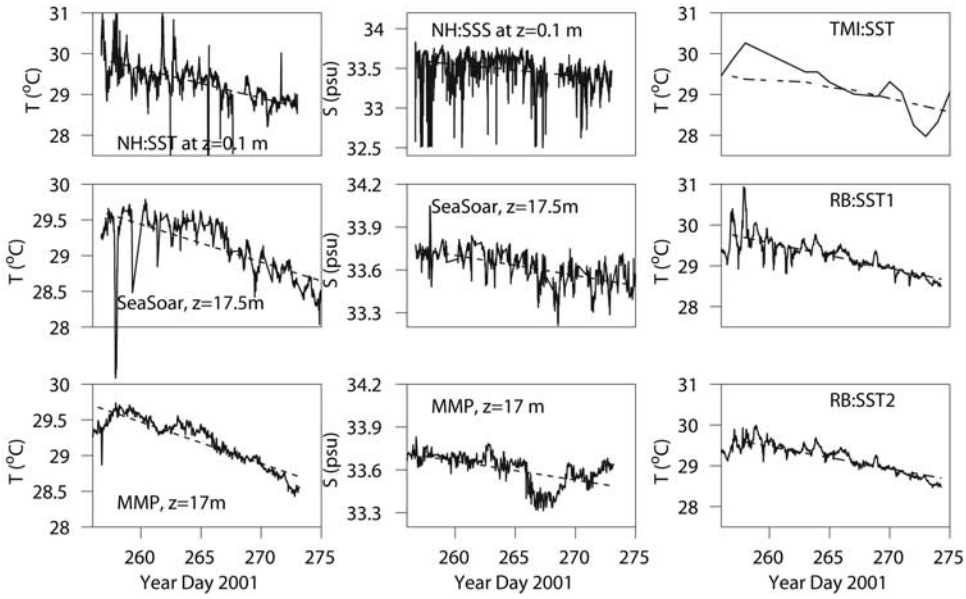

Figure 11. (left) Times series of temperature and salinity with the corresponding linear regression lines at 0.1 m, 17.5 m, and 17 m; T and S at 0.1 m and 17.5 m were from the *New Horizon*, and T and S at 17 m were from the *Ron Brown*. (right) SST tendencies are from TMI and R/V *Ron Brown*. The slope of the 19 day regression lines (dash lines) was used as the temporal rate of change at that depth.

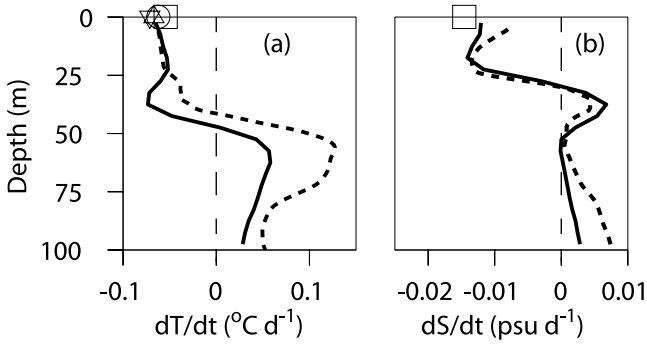

Figure 12. Temporal rate of change of (left) temperature and (right) salinity as a function of depth from SeaSoar (solid lines) and MMP (dashed lines). The open squares are the estimates from 0.1 m *T* and *S* (R/V *New Horizon*). The triangle denotes the estimate from TMI. The time rate of change of SST from the R/V *Ron Brown* is marked with an open circle and a star.

of the butterfly pattern (Figures 11 and 12). Near-surface salinity at 0.1 m depth decreased at a rate of 0.015 psu d^{-1} based on *New Horizon* measurements at a depth of 0.1 m (Figures 11 and 12).

4.3. Horizontal Gradients and Horizontal Velocity

[40] Computation of the horizontal advection of heat and salt at the center of the butterfly pattern requires horizontal velocity and horizontal gradients of temperature and salinity at the center (equations (2) and (3)). As discussed below, horizontal gradients of *T* and *S* were estimated by two different methods from SeaSoar and MMP hydrographic measurements. Velocity components were obtained from ship-mounted ADCP measurements and, in addition, geostrophic velocity was estimated from SeaSoar hydrography and Ekman velocity from surface winds.

4.3.1. Horizontal Gradients

4.3.1.1. Method 1

[41] Time series of horizontal gradients at the center of the butterfly pattern were constructed from SeaSoar sections by assuming that space-depth sections of *T* and *S* were quasi-steady in time. SeaSoar produced 11 zonal depth (*x*-*z*) and meridional depth (*y*-*z*) sections. The length and depth of each transect was 146 km and 200 m, respectively. Individual (*x*-*z*) and (*y*-*z*) sections were separated by about 34.5 hours. Gradients were estimated for each transect by a linear least squares fit through the data in each 5 m depth bin along the transect (Figures 13a and 13b). The slope of the linear fit was taken as the gradient at that depth for the transect, and the resulting time-depth fields of meridional and zonal gradients of *T* and *S* at the center of the butterfly pattern along with corresponding gradients of SST from TMI are illustrated in Figures 14 and 15.

[42] Cruise-averaged temperature gradients were small and nearly constant in the upper 20 m, but were large below 20 m (Figures 14 and 15). The cruise-averaged meridional and zonal temperature gradients in the upper 20 m were near

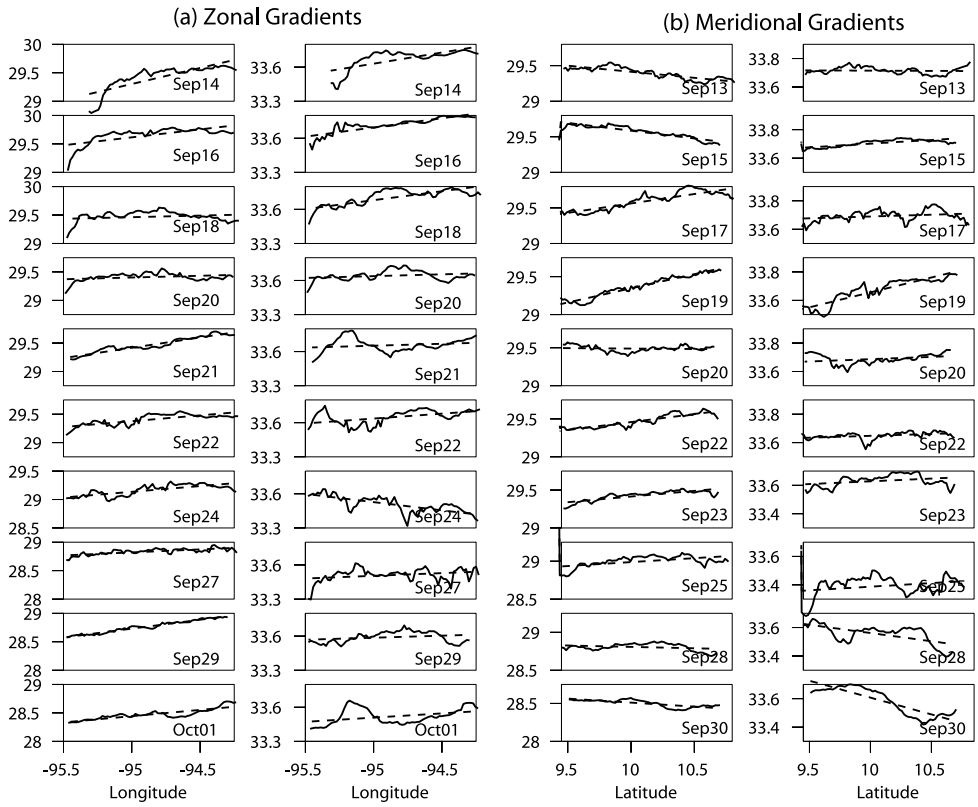

Figure 13. (a) Zonal gradients and (b) meridional gradients: (left) temperature and (right) salinity horizontal profiles with the corresponding linear regression lines at a depth of 12.5 m. The slopes of the 146 km regression lines were used as the gradient at that depth (method 1).

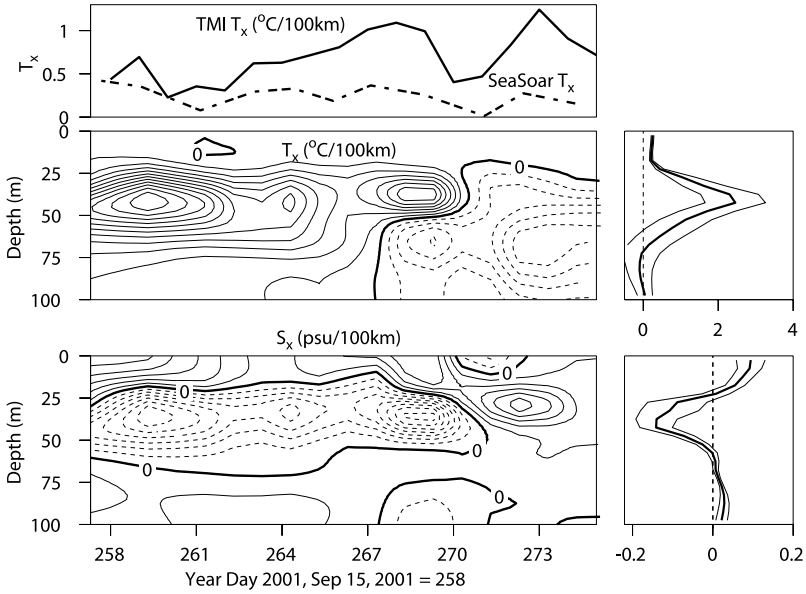

Figure 14. Zonal gradients of *T* and *S* as a function of time and depth along with cruise averages (in the right panels) estimated by method 1. Units are in °C/100 km and psu/100 km, respectively. Contour intervals are 0.5°C/100 km and 0.05 psu/100 km. Dashed lines denote negative gradients, and solid lines denote positive gradients. The cruise-averaged profiles appear in the right panels; thin lines denote standard error estimates. The top panel shows zonal gradients of temperature from TMI data and from the 2.5 m depth SeaSoar observations.

zero and about 0.2°C/100 km, respectively. Salinity gradients were more variable than temperature gradients in the upper 20 m (Figures 14 and 15), caused by variability in surface rainfall. The high degree of spatial and temporal variability of surface rainfall caused significant salinity variations on scales shorter than 146 km as can be seen in the salinity records at a depth of 12.5 m (Figure 13).

[43] Gradients of SST from TMI (Figures 14 and 15) were computed similarly to those from the SeaSoar observations, except that they were estimated over a larger distance (220 km) than the SeaSoar sections (146 km). Least square fits to 10 TMI SST estimates, each separated by 25 km in the zonal and meridional directions, were computed for each 3 day averaging interval of the TMI data. The mean location of the 10 zonal and 10 meridional TMI SST measurements was 9.875°N and 94.875°W. The resolution of the TMI temperature data was 40–50 km.

[44] The meridional SST gradient from TMI and the upper 5 m gradient from SeaSoar agreed very well, while the zonal SST gradient from TMI was a factor of 3 larger than that from SeaSoar (Figures 14 and 15). The difference between zonal TMI and SeaSoar gradients was even larger when the TMI gradients were estimated over a distance (six points, 170 km) more nearly comparable to the length of the SeaSoar sections (146 km). The cause of the difference between the zonal TMI and SeaSoar temperature gradients is uncertain. It seems unlikely that the horizontal temperature gradient at the surface could be systematically different from the gradient vertically averaged over the upper 5 m; the cruise-averaged horizontal gradients of temperature from SeaSoar show negligible variation as a function of depth in the upper 20 m (Figures 14 and 15). Daytime heating of a shallow surface layer may cause the surface temperature to exceed the temperature at 2–3 m depth by more than 1°C, which could cause the TMI 3 day averaged gradients to be biased if TMI pixels are averaged over different portions of a day. Rainfall tends to stratify the surface layer and could enhance the temperature difference between the surface and upper 5 m average. Because the budget calculations do not depend on TMI temperature, a definitive explanation for the difference between the TMI and SeaSoar temperature gradients is beyond the scope of this paper.

[45] Despite the uncertainty in the accuracy of the TMI temperature gradients, the cruise-averaged TMI temperature pattern (Figure 2) is qualitatively consistent with the average SeaSoar gradients and, together with the cruise-averaged sea surface height field, provides a larger-scale context for interpreting the results of the budget calculations.

4.3.1.2. Method 2

[46] Spatial gradients of *T* and *S* as a function of time and depth were also computed by combining time series measurements at the center of the butterfly from MMP and measurements at the end points of the butterfly from SeaSoar. Hourly averaged measurements were used to construct these time series, i.e., 1 hour intervals at the ends of the butterfly sections and at the center of the butterfly. Although this method allowed us to compute spatial gradients between the end points and the center of the butterfly with measurements over the same time interval, the time series of the gradients contained more high-frequency variability (noise) than the gradients estimated by method 1. The source of the additional noise was the neglect of ~80% of the data along the transects and the estimation of gradients over a shorter distance (~65 km) rather than the full length of the section (146 km).

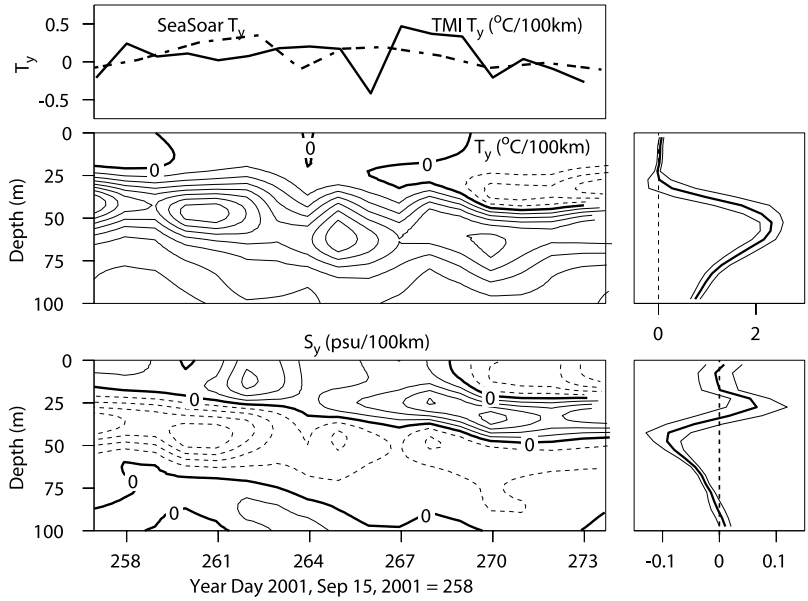

Figure 15. Meridional gradients of *T* and *S* as a function of time and depth long with cruise averages (in the right panels) based on method 1. Units are in °C/100 km and psu/100 km, respectively. Contour intervals are 0.5°C/100 km and 0.05 psu/100 km. Dashed lines denote negative gradients, and solid lines denote positive gradients. The cruise-averaged profiles appear in the right panels; thin lines denote standard error estimates. The top panel shows meridional gradients of temperature from TMI data and from the 2.5 m depth SeaSoar observations.

[47] The cruise-averaged spatial gradients as a function of depth are shown in Figure 16. It appears that on average both methods 1 and 2 produced comparable magnitudes and vertical structure of spatial gradients of *T* and *S* (Figures 14–16). Temperature gradients and their standard error (i.e., standard deviation/(number of samples)$^{1/2}$) were small in the upper 20 m for both methods, whereas the salinity gradients have large standard errors in the upper 20 m as the result of spatial patchiness in rainfall (Figure 16). Spatial gradients of salinity in the upper 15 m from method 1 are nearly constant in the upper 15 m, which is physically realistic because of strong vertical mixing near the surface. Spatial gradients of S from method 2 exhibit considerable variations with depth in the upper 15 m, which is not physically realistic.

[48] Horizontal gradients from method 1 were used for the budget calculations discussed below because (1) there are no systematic differences between spatial gradients of *T* and *S* computed by the two methods in the upper 20 m, (2) method 2 yields noisier estimates than method 1, and (3) method 1 produces more physically realistic vertical variations of salinity gradients in the upper 15 m.

4.3.2. Horizontal Velocity

4.3.2.1. Total Velocity

[49] ADCPs measure total horizontal velocity, which includes Ekman, geostrophic, tidal and internal wave components. ADCP observations were made between 15 and 250 m depth; near-surface velocity was estimated by extrapolating the observed velocity at 15 m depth to the surface by assuming that vertical shear in the upper 25 m was constant. We also estimated near-surface velocity by assuming that vertical shear was zero above 15 m depth. The difference in heat and salt advection based on these two near-surface velocity estimates was less than 3% in the advection terms, which is small compared to other uncertainty. As mentioned above, variations in horizontal currents

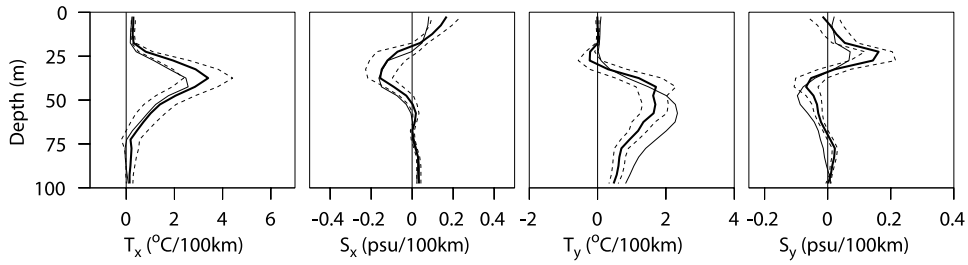

Figure 16. Cruise-averaged zonal and meridional gradients of *T* and *S* from method 2 (bold solid lines). Dashed lines denote standard error estimates. Thin solid lines represent the cruise mean gradients from method 1 (see also Figures 14 and 15).

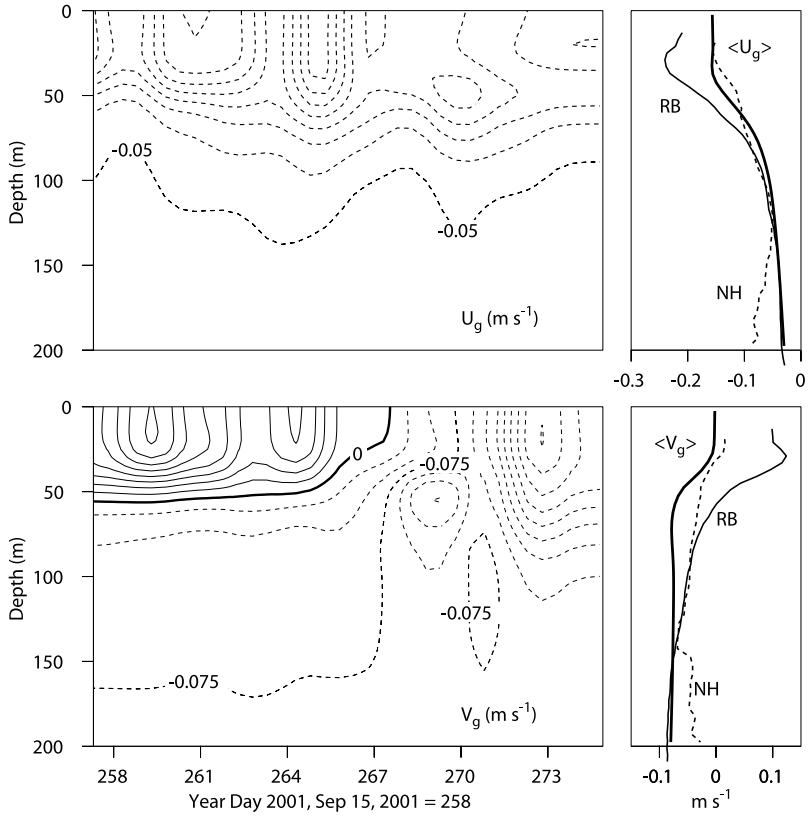

Figure 17. Geostrophic velocity (top) U_g and (bottom) V_g as a function of time (in the left panels). Units are in m s^{-1}, and the contour interval is 0.025 m s^{-1}. Cruise-averaged geostrophic velocity, $\langle U_g \rangle$, $\langle V_g \rangle$ (bold solid line) along with cruise-averaged ADCP velocities from R/V *Ron Brown* (RB) (thin solid line) and R/V *New Horizon* (NH) (thin dashed line) are shown in the right panels.

were dominated by near-inertial oscillations (Figure 6), which were low-pass filtered before computing the advection of heat and salt.

4.3.2.2. Geostrophic Velocity

[50] Geostrophic velocity was calculated from the SeaSoar density sections and referenced to the *Ron Brown*'s ADCP measurements at a depth of 200 m. The thermal wind equations,

$$\rho_0 f \frac{\partial U_g}{\partial z} = g \frac{\partial \rho}{\partial y} \tag{9a}$$

$$\rho_0 f \frac{\partial V_g}{\partial z} = -g \frac{\partial \rho}{\partial x}, \tag{9b}$$

were used to estimate the geostrophic velocity shear, where ρ is the density of seawater; ρ_0 is the average density of the record; g is the acceleration due to gravity; f is the inertial frequency, and U_g and V_g are geostrophic velocity components in zonal and meridional directions, respectively. Horizontal gradients of density were obtained by the same method (method 1) used to estimate T and S gradients. The geostrophic velocity relative to 200 m was computed by vertically integrating the geostrophic shear given in equations (9a) and (9b), and the absolute geostrophic velocity was obtained by adding the cruise-averaged ADCP velocity from R/V *Ron Brown* at a depth of 200 m (level of known motion).

[51] Geostrophic velocity from the average horizontal density gradients over the butterfly was qualitatively consistent with the observed ADCP velocity (Figures 8 and 17); for example, the zonal component, U_g was westward while the meridional component V_g was northward at the beginning of the experiment and turned southward about halfway through the experiment. The observed geostrophic and ADCP velocities are consistent with the westward movement of an anticyclonic eddy (Figure 2).

4.4. Vertical Velocity

[52] The computation of vertical advection of heat and salt requires vertical velocity and vertical gradients of T and S. Vertical gradients of T and S were obtained by 10 m center differencing of transect-averaged profiles from SeaSoar (Figure 8). Vertical velocity was estimated by three different methods: (1) Ekman pumping driven by the curl of the wind stress, (2) integration of the divergence of horizontal velocities, and (3) use of the conservation of mass equation.

4.4.1 Ekman Pumping

[53] Climatological wind records show moderate wind stress curl over the northeast tropical Pacific Ocean, and a semipermanent upwelling feature, the "Costa Rica dome" centered near 9°N, 90°W [*Wyrtki*, 1964; *Hofmann et al.*, 1981; *Umatani and Yamagata*, 1991; *Kessler*, 2002]. The strength and the position of this oceanic feature depend on the temporal and spatial variability of surface winds

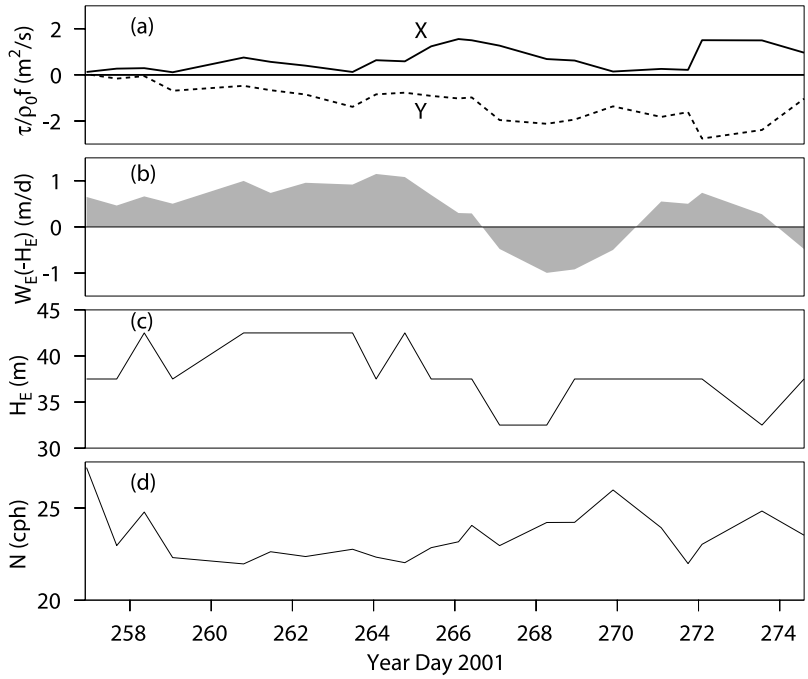

Figure 18. (a) Zonal and meridional components of Ekman transport. (b) Vertical velocity at depth H_E estimated from the curl of the wind stress. (c) H_E, the depth at which buoyancy frequency was a maximum. For an Ekman depth (H_E) of 38 m, $<U_E> = 0.02$ m s^{-1} (eastward) and $<V_E> = -0.03$ m s^{-1} (southward). Wind stress gradients at 10°N, 95°W were estimated from 3 day averaged QuikSCAT data. (d) Buoyancy frequency N at depth H_E.

[e.g., *Umatani and Yamagata*, 1991]. The Ekman pumping velocity does not include vertical motions associated with mesoscale eddies observed during EPIC (Figure 2) [*Raymond et al.*, 2004].

[54] Upwelling velocity just below the mixed layer was estimated by use of

$$W_E(-H_E) = \frac{\nabla \times \tau}{\rho_0 f}, \tag{10}$$

where H_E is the depth at which the vertical density gradient is largest, τ is the wind stress; $\rho_0 = 1000$ kg m^{-3}, and $f = 2\Omega \sin(10°) = 2.53 \times 10^{-5}$ s^{-1} (inertial period = 68.9 hours). Three day averaged QuikSCAT wind stresses were used to compute W_E (Figure 18). Wind stress gradients were estimated over 150 km, which was comparable to the extent of the SeaSoar survey pattern. Vertical velocity above the depth of H_E was assumed to decrease linearly to zero at the surface:

$$W_E(z) = \left(\frac{-z}{H_E}\right) W_E(-H_E). \tag{11}$$

The cruise-averaged $\langle H_E \rangle$ was 38 m.

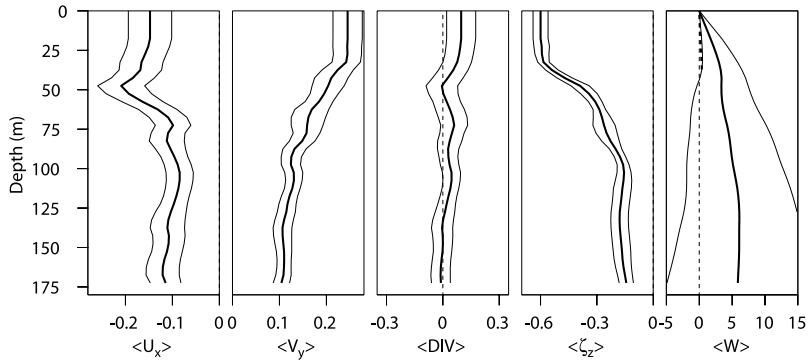

Figure 19. Cruise-averaged zonal and meridional gradients of U, V, and divergence and the vertical component of relative vorticity, ζ_z, and estimated vertical velocity, W, in the upper 200 m from *New Horizon*'s ADCP. Units are in d^{-1} for gradient terms and in m d^{-1} for vertical velocity. Horizontal gradients for a given depth were obtained from linear regression. Thin lines denote standard error estimates. Vertical velocity based on Ekman pumping (bold dashed line) is also shown in the right panel.

[55] Ekman transport was toward the southeast (Figure 18). For an Ekman depth (H_E) of 38 m, the resulting Ekman velocity was 0.03 m s^{-1}, which was approximately 10% of the cruise-averaged near-surface velocity from the ADCP on R/V *Ron Brown*. Therefore it was unlikely that Ekman transport played a significant role in the advection of heat and salt.

4.4.2. Divergence

[56] Vertical velocity as a function of depth was also obtained by vertically integrating the continuity equation from a specified depth z to the surface (Figure 19):

$$W_A(z) = \int_{-z}^{0} \left(\frac{\partial U}{\partial x} + \frac{\partial V}{\partial y} \right) dz'. \tag{12}$$

Horizontal gradients (linear trends) of U and V were constructed from cruise-averaged butterfly sections of U and V by use of the same method used to estimate horizontal gradients of T and S (method 1). Cruise-averaged sections of horizontal velocity gradients were used to estimate divergence to minimize uncertainties due to inadequate sampling and due to high-frequency velocity fluctuations associated with internal waves and barotropic tides. The velocity divergence at the center of the butterfly was positive in the upper 35 m, and was nearly zero below 50 m. As shown in Figures 18 and 19, the Ekman pumping and divergence estimates of vertical velocity both show upwelling, though W_A is significantly larger than W_E; W_A is a factor of 8 larger than W_E at 25 m depth. The error bars on W_A are quite large and a cruise-averaged magnitude of up to 3 m d^{-1} in the upper 50 m, though large, is only one-tenth the magnitude found at an open ocean front [*Pollard and Regier*, 1992].

[57] The vertical component of relative vorticity, ζ_z was negative in the upper 200 m (Figure 19), consistent with rotation of an anticyclonic eddy (Figure 2). The cruise-averaged surface geostrophic velocity of the eddy was estimated from the information in Figure 2. The radius r of the eddy was about 100 km and the change in surface height from the center to r = 100 km was about 0.12 m (upper limit of the range from 0.06 to 0.12 m). Applying geostrophic theory, the tangential velocity at r = 100 km is 0.5 m/s and the relative vorticity of the eddy at the surface was -0.8 d^{-1}, which is in reasonable agreement with -0.6 d^{-1} computed from the *New Horizon* ADCP measurements (Figure 19). The ratio of relative vorticity to the Coriolis parameter f is the Rossby number, which equals 0.27 when computed from the ADCP relative vorticity. This value is sufficiently large that one might expect departures from geostrophy.

4.4.3. Conservation of Mass

[58] Vertical velocity may also be estimated from the conservation of mass equation for incompressible flow (the total derivative of density equal to zero). If one substitutes mean and fluctuating components for each of the variables, averages the equation and solves for the mean vertical velocity, one obtains

$$W_M = -\left[\frac{\partial \rho}{\partial z}\right]^{-1} \left[\frac{\partial \rho}{\partial t} + U\frac{\partial \rho}{\partial y} + V\frac{\partial \rho}{\partial y}\right], \tag{13}$$

where each variable is an average over the cruise and turbulent transport and radiative modification of density have been neglected. Equation (13) is not valid in the surface mixed layer, where the vertical density gradient is small, turbulent transport may be large, and the absorption of solar radiation may be significant. W_M was evaluated from SeaSoar measurements of density and *Ron Brown* ADCP measurements of U and V over 5 m vertical intervals in the same manner as described above. The vertical profile of W_M plotted in Figure 20 shows a maximum of about 1 m d^{-1} (upwelling) at a depth of 27.5 m. The profile is assumed to be decrease linearly to zero at the surface above the 27.5 m level. The value of W_M at 25 m depth is about three times as large as the estimate of vertical velocity due to Ekman pumping (Figure 18) and about one-third of the divergence estimate (Figure 19).

4.5. Heat Advection and the Heat Budget

[59] Time-depth sections of the zonal advection of heat by total velocity, $-\rho C_p U \partial T/\partial x$, and by geostrophic velocity, $-\rho C_p U_g \partial T/\partial x$, are shown in Figures 21 and 22 together with corresponding sections of meridional and vertical heat advection. These sections illustrate that heat advection below 20 m depth was large and variable in comparison to the upper 20 m. This variability, some of which was error associated with unresolved motions and gradients, leads to large uncertainties in estimating advective fluxes in the pycnocline, which grow with increasing depth below 20 m. As a result, meaningful heat and salt budgets can only be calculated in the weakly stratified layer above the pycnocline. The budgets of heat and salt were computed for the 0–20 m and 0–25 m layers, where the three advective terms were relatively small. The bases of both layers were below the mean depth of the mixed layer (12 m from MMP profiles (Table 1)), and well above the mean depth of maximum stratification (38 m from Figures 5, 8, and 18).

[60] Cruise-averaged advective fluxes of heat determined by various methods were in good agreement in the upper 20 m of the water column and were qualitatively similar below 20 m (Figures 21 and 22). The zonal cruise-averaged advection of heat was small and positive in the upper 20 m for both the total velocity and geostrophic velocity estimates, which tended to warm the surface layer. The estimates of meridional advection of heat by total velocity, $-\rho C_p V \partial T/\partial y$, and by geostrophic velocity, $-\rho C_p V_g \partial T/\partial y$, were near zero in the upper 20 m. Zonal advection was large and positive and meridional advection was large and negative in the highly stratified layer below 20 m.

[61] Below 20 m there were significant differences between cruise-averaged profiles of horizontal heat advection estimated from the mean velocity times the mean temperature gradient, ($\langle U \rangle \langle \partial T/\partial x \rangle$ and $\langle V \rangle \langle \partial T/\partial y \rangle$) and from the average of the products ($\langle U \partial T/\partial x \rangle$ and $\langle V \partial T/\partial y \rangle$), which includes contributions to advection due correlations between horizontal velocity and the temperature gradient. The cruise-averaged estimates by both methods were similar in magnitude in the upper 20 m (Figure 21); however estimates tended to deviate in the pycnocline below 20 m, particularly in the meridional component, suggesting that correlations between the merdional velocity and temperature gradient may have been important. The difference may

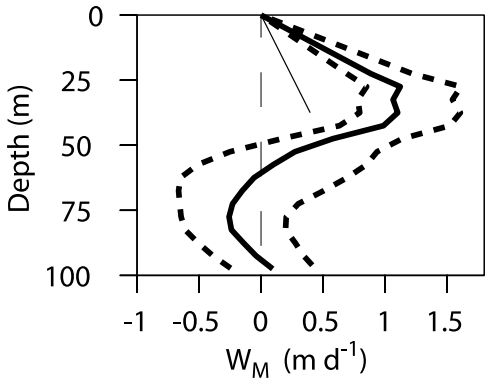

Figure 20. Cruise-averaged vertical velocity, W_M, estimated from equation (13). Dashed lines are the standard error estimates. Ekman pumping velocity, W_E(z) (equation (11)), is shown as a solid line.

also be due to errors, because $\langle V\partial T/\partial y\rangle$ is noisier (Figure 21) than the product of the means.

[62] Vertical heat advection based on Ekman pumping, $-\rho C_p W_E \partial T/\partial z$, conservation of mass, $-\rho C_p W_M \partial T/\partial z$, and velocity divergence, $-\rho C_p W_A \partial T/\partial z$, varied greatly in magnitude below 20 m depth (Figure 21). The cruise-averaged heat advection, resulting from upwelling and the positive vertical gradient of T, tended to cool the upper ocean. There was no significant difference between $-\rho C_p \langle W_E \partial T/\partial z\rangle$ and $-\rho C_p \langle W_E\rangle\langle \partial T/\partial z\rangle$, i.e., there was no correlation between wind stress curl and the vertical gradient of T for 3 day averages of each variable. The magnitude of vertical heat advection based on Ekman pumping may have been an incorrect estimate of the true advection because it did not include vertical velocity associated with internal motions that were not driven by the local wind stress. In the budget computations that follow, vertical velocity from the measured divergence was used because it tends to give better agreement between heat and freshwater budgets for the 0–20 and 0–25 m layers.

[63] Heat advection was integrated (equation (2)) over the 0–20 and 0–25 m layers and the components for the various measurements and methods are presented in Tables 2a and 2b. Estimates of horizontal heat advection based on the average product of velocity times the temperature gradient are intrinsically more uncertain than the product of cruise-mean velocity times the cruise-mean temperature gradient; this uncertainty is reflected in the relatively large differences between estimates (A_1 and B_1 in Table 2a) from the *Ron Brown* and *New Horizon* ADCP velocity measurements. Estimates of horizontal heat advection based on the product of cruise-mean velocity times cruise-mean temperature gradient (A_2 and B_2 in Table 2a) are in better agreement, although they may be biased because correlations between velocity and temperature gradient are neglected. An estimate of the bias based on the ADCP velocity from the *Ron Brown* and geostrophic velocity (Table 2a) suggests that heat advection based on the product of the mean velocity times the mean gradient is

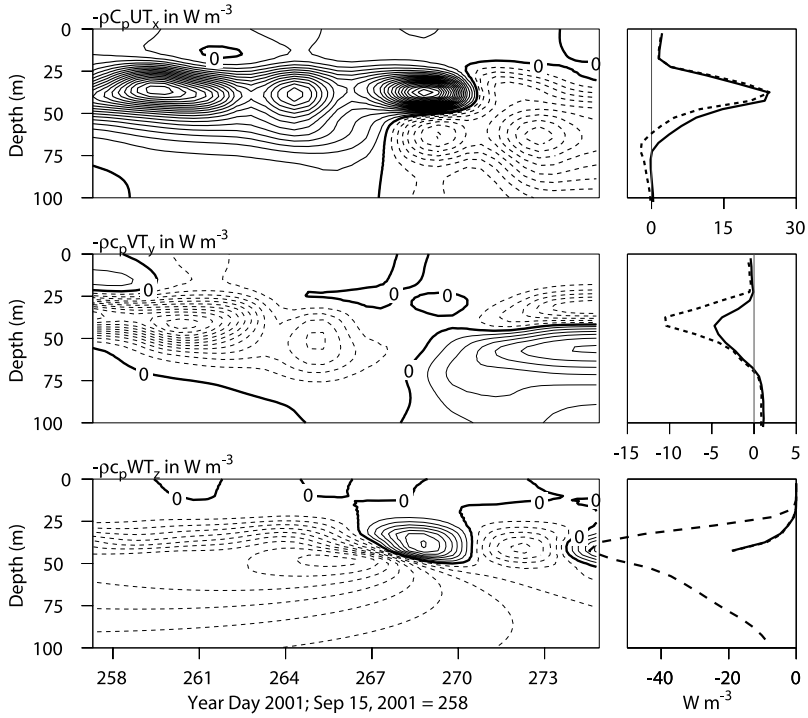

Figure 21. Vertical distribution of heat advection per unit depth (W m^{-3}). Solid contours denote positive heat fluxes, and dashed contours denote negative heat fluxes (left panels). (top) Zonal advection, (middle) meridional advection, and (bottom) vertical advection based on W_E are all shown. The contour interval is 2.5 W m^{-3}. Cruise-averaged advection of heat per unit depth (W m^{-3}) appears in the right panels. The long dashed line in the bottom panel denotes vertical advection based on $W_A \langle \partial T/\partial z\rangle$. The short dashed line indicates the mean $\langle u\nabla T\rangle$, and the solid line indicates $\langle u\rangle \langle \nabla T\rangle$.

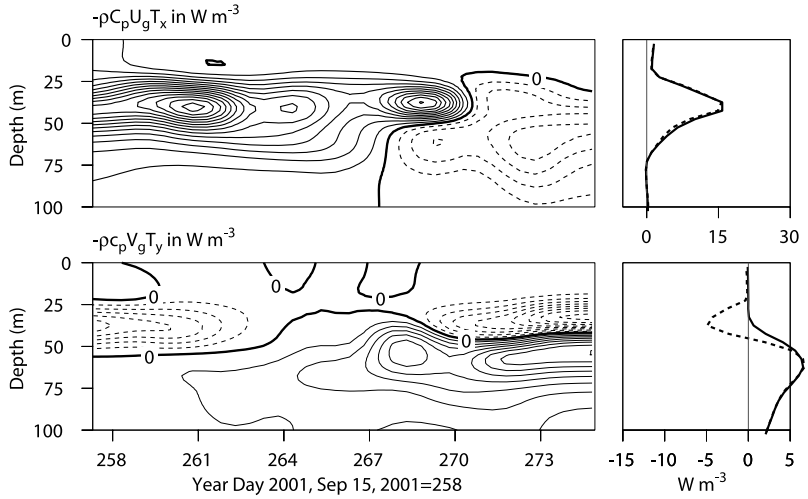

Figure 22. Vertical distribution of heat advection per unit depth (W m^{-3}) by geostrophic velocity. Solid contours denote positive heat fluxes, and dashed contours denote negative heat fluxes (right panels). (top) Zonal advection and (bottom) meridional advection are both shown. The contour interval is 2.5 W m^{-3}. Cruise-averaged advection of heat per unit depth (W m^{-3}) is shown in the left panels. The short dashed line indicates the mean $\langle u_g \nabla T \rangle$, and the solid line indicates $\langle u_g \rangle \langle \nabla T \rangle$.

biased high by 5 and 7 W m^{-2} for the 20 and 25 m layers, respectively. In the heat budget calculation that follows, we opted to use the product of the mean velocity times the mean gradient from both the *Ron Brown* and *New Horizon* velocity measurements, because this estimate was more statistically reliable. A correction for the bias was then applied.

[64] Estimates of horizontal heat advection based on the geostrophic velocity were smaller, on average, than those based on the ADCP measurements, but they were highly correlated with the *Ron Brown* estimates. The geostrophic velocity, and the resulting advection, may be biased low because it did not include Ekman transport and other ageostrophic motions and because the calculation of geostrophic velocity was based on horizontal density gradients averaged over 146 km. Smoothing density gradients over this distance may underestimate the true density gradient at the center and, hence, the geostrophic velocity at the center of the butterfly pattern.

[65] The cruise-averaged net surface heat flux was estimated by adding all of the components of the heat budget (equation (2)) for the 0–20 and 0–25 m layers (Table 3). The dominant term for both layers is the storage term, but all other terms are significant. The uncertainty in each component is given in square brackets. In most cases, the uncertainty is based on calculation of the component from different data. The uncertainty for the turbulent heat flux at the base of the layer is the 70% confidence interval based on the bootstrap method [*Efron and Gong*, 1993] applied to the dissipation data. The uncertainty in penetrative radiation through the base of the layers was less than 1 W m^{-2} and is therefore omitted. The error estimates for the net surface heat flux are approximately the standard error, but may be underestimated, particularly for the 25 m layer, because an error estimate for vertical heat advection was not included. The correction for bias in the horizontal heat advection is discussed above.

[66] Vertical heat advection, which tended to compensate horizontal advection, is a small term in the 0–20 m layer, but it is comparable to horizontal advection in the 0–25 m layer. Vertical heat advection is perhaps the most uncertain component of the budget (Tables 2b and 3) for the 25 m

Table 2a. Cruise-Averaged Horizontal Advection of Heat[a]

	0–20 m Layer				0–25 m Layer			
Horizontal Advection, W m^{-2}	RB	NH	RB-NH	GV	RB	NH	RB-NH	GV
$A_1 = -\int_{-h}^{0} \rho c_p \langle U \frac{\partial T}{\partial x} \rangle dz$	34.4	6.2	20.3	23.6	55.4	24.2	39.8	36.4
$A_2 = -\int_{-h}^{0} \rho c_p \langle U \rangle \langle \frac{\partial T}{\partial x} \rangle dz$	34.7	28.0	31.3	25.5	54.6	45.4	50.0	38.8
$B_1 = -\int_{-h}^{0} \rho c_p \left\langle V \frac{\partial T}{\partial y} \right\rangle dz$	−10.8	−1.9	−6.3	−3.8	−13.3	−4.5	−8.9	−5.4
$B_2 = -\int_{-h}^{0} \rho c_p \langle V \rangle \left\langle \frac{\partial T}{\partial y} \right\rangle dz$	−5.0	−2.0	−3.5	−0.8	−5.3	−2.1	−3.7	−0.9
Total: $A_1 + B_1$	24	4	14	20	42	20	31	31
Total: $A_2 + B_2$	29	26	28	25	49	43	46	38

[a]RB and NH denote flux estimates from the R/V *Ron Brown* acoustic Doppler current profiler (ADCP) and the R/V *New Horizon* ADCP, respectively. GV denotes flux estimates by use of geostrophic velocity. Averages of RB and NH advective fluxes are given in the RB-NH column.

Table 2b. Cruise-Averaged Vertical Advection[a]

Vertical Advection, Wm^{-2}	0–20 m Layer	0–25 m Layer
$C_1 = -\int_{-h}^{0} \rho c_p \langle W_E \frac{\partial T}{\partial z} \rangle dz$	−1	−5
$C_2 = -\int_{-h}^{0} \rho c_p \langle W_E \rangle \langle \frac{\partial T}{\partial z} \rangle dz$	−1	−4
$C_3 = -\int_{-h}^{0} \rho c_p \langle W_M \rangle \langle \frac{\partial T}{\partial z} \rangle dz$	−2	−17
$C_4 = -\int_{-h}^{0} \rho c_p \langle W_A \rangle \langle \frac{\partial T}{\partial z} \rangle dz$	−5	−40

[a]The vertical temperature gradient was from SeaSoar data.

layer because of the large uncertainty in W_A (Figure 19). Vertical heat advection based on vertical velocity W_A from integration of the horizontal velocity divergence was chosen for the budget to minimize differences between estimates of net surface heat flux for the 20 and 25 m layers. The choice of vertical velocity based on conservation of mass would result in net surface heat fluxes of 42 and 66 W m^{-2} for the 20 and 25 m layers, respectively; the choice has a minor effect on the 20 m layer, but a large effect on the 25 m layer.

[67] The cruise-averaged net surface heat flux was 39 and 43 W m^{-2} upward for the 0–20 and 0–25 m layers, respectively, or a mean of 41 ± 8 W m^{-2}, which may be compared to 30 W m^{-2} measured on the *Ron Brown* near the center of the butterfly pattern over the same period (Hare et al., submitted manuscript, 2005).

4.6. Salinity Advection and the Freshwater Budget

[68] Components of salinity advection as a function of time and depth were computed similarly to heat advection; time-depth sections of salinity advection are shown in Figures 23 and 24. Zonal and meridional salinity advection were large and variable in the upper 20 m and in the strongly stratified pycnocline. This differs from horizontal heat advection, which was relatively small and constant in the upper 20 m compared to the pycnocline (Figures 21 and 22). The difference was due to high tropical rainfall in the region that caused a higher degree of temporal and spatial variability of salinity than temperature in the upper 20 m; rainfall rates are much more variable in space and time than surface heat fluxes. The patterns of horizontal advection of salinity by total and geostrophic velocity were very similar for both the zonal and meridional components, although the magnitudes of the geostrophic advection were larger. The vertical advection of salt due to Ekman pumping was near zero in the upper 20 m (Figure 23), which is not surprising because vertical velocity and the vertical gradient of salinity are both small in this layer. The magnitude and variability of vertical salt advection was large in the pycnocline below the 20 m layer.

[69] Cruise averaged advective fluxes of salt determined by various methods are plotted in Figures 23 and 24. The zonal component based on the product of the mean velocity times the mean salinity gradient ($\langle U \rangle \langle S_x \rangle$) was nearly the same as the component based on the mean product of velocity times the salinity gradient ($\langle U S_x \rangle$) in the upper 30 m and very similar below that. The same was true for zonal advection computed from the zonal component of geostrophic velocity (Figure 24). The cruise-averaged meridional salt advection based on the product of the means ($\langle V \rangle \langle S_x \rangle$) was significantly different from salt advection based on the mean product ($\langle V S_x \rangle$) in the upper 40 m (Figure 23) and the same was true for salt advection from the meridional component of geostrophic velocity (Figure 24). The difference implies that there were significant correlations between the meridional velocity component and meridional salinity gradient. The vertical variation of horizontal salt advection computed from total velocity (Figure 23) was similar to that computed from geostrophic velocity, although the magnitude of the advection from geostrophic velocity was less than that from total velocity.

[70] Cruise-averaged vertical salt advection based on Ekman pumping, conservation of mass, and horizontal velocity divergence varied greatly in magnitude below 20 m depth (Figure 23). As stated above, vertical salt advection based on vertical velocity from the measured horizontal velocity divergence was used to minimize the difference between surface evaporation minus precipitation ($E - P$) computed for the 0–20 m and 0–25 m layers (see below). This choice also minimized the difference between surface heat flux computed for the 20 and 25 m layers (Table 3).

[71] Salt advection was integrated (equation (3)) over the 0–20 and 0–25 m layers and the components of freshwater advection from the various measurements and methods are presented in Tables 4a and 4b. The values for freshwater advection presented in Table 4 are analogous to values for heat advection in Table 2 and the discussion of the components of heat advection in the previous section applies also to the components of freshwater advection in Table 4. The values chosen from Table 4 to estimate evaporation minus precipitation at the surface were entirely analogous to the values chosen from Table 2 to estimate the surface heat flux for the 0–20 and 0–25 m layers (Table 3). Horizontal advection from the product of the mean velocity times the mean salinity gradient ($D_2 + E_2$) averaged over the two ships (RB-NH) was used for the freshwater budget. This

Table 3. Cruise-Averaged Heat Budget[a]

Terms in Equation (2), W m^{-2}	0–20 m	0–25 m
Mean time rate of change, $-\int_{-h}^{0} \rho c_p \langle \frac{\partial T}{\partial t} \rangle dz$; individual estimates from RB and NH are given in brackets	+57 [54, 59]	+69 [66, 71]
Mean turbulent heat flux at depth h: $F_T(-h)$; standard error estimates are given in brackets	−18 [−15, −21]	−13 [−14, −12]
Total mean advection: [mean $(A_2 + B_2)$] + C_4; within brackets are RB and NH estimates	+23 [21, 24]	+6 [3, 9]
Horizontal advection bias correction	−5	−7
Mean penetrative solar radiation: $R(-h)$	−18	−12
Net surface heat flux: Q_S	+39 [±8]	+43 [±7]

[a]The quantities in brackets are upper and lower bounds from different estimates or, in the case of turbulent heat flux and the net surface heat flux, the approximate standard error estimate. Cruise-averaged net surface heat flux from *Ron Brown* data sets is 30 W m^{-2} (Hare et al., submitted manuscript, 2005).

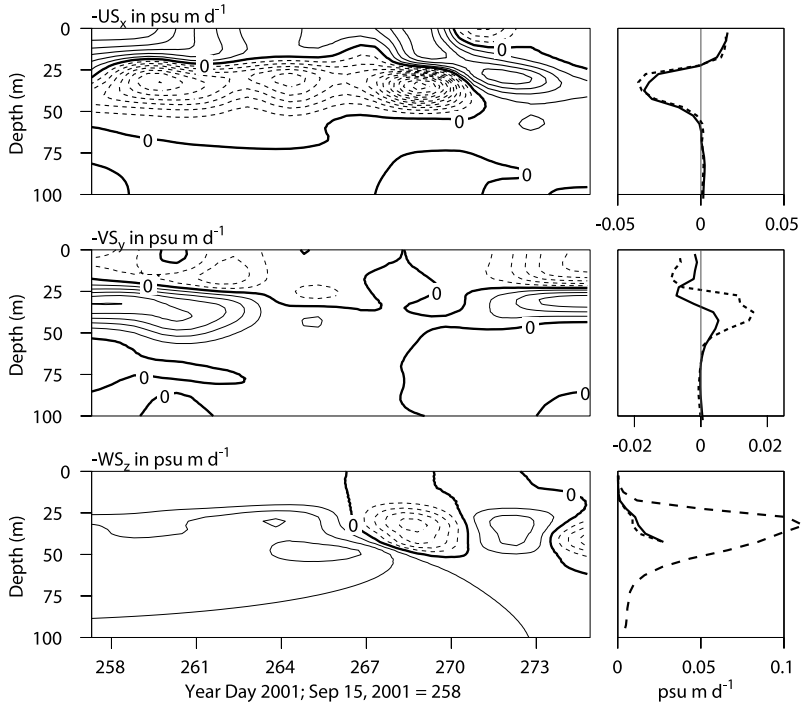

Figure 23. Vertical distribution of salinity advection per unit depth (psu m d^{-1}). Solid contours denote positive salinity fluxes, and dashed contours denote negative salinity fluxes (left panels). (top) Zonal advection, (middle) meridional advection, and (bottom) vertical advection based on W_E are all shown. The contour interval is 0.01 psu m d^{-1}. Cruise-averaged advection of salinity per unit depth (psu m d^{-1}) appears in the right panels. The long dashed line in the bottom panel denotes vertical advection based on W_A $\langle \partial S/\partial z \rangle$. The short dashed line indicates the mean $\langle u\ \nabla S \rangle$, and the solid line indicates $\langle u \rangle$ $\langle \nabla S \rangle$.

estimate was biased because of correlation between horizontal velocity and horizontal salinity gradient. A correction for this bias was obtained from the average difference between the mean product (D_1 + E_1) and the product of the means (D_2 + E_2) from the *Ron Brown* velocity and the geostrophic velocity. The *Ron Brown* and geostrophic velocity estimates of horizontal freshwater advection are highly correlated and the bias from each was 3 mm d^{-1}. A correction for the bias was included in the freshwater budget discussed below.

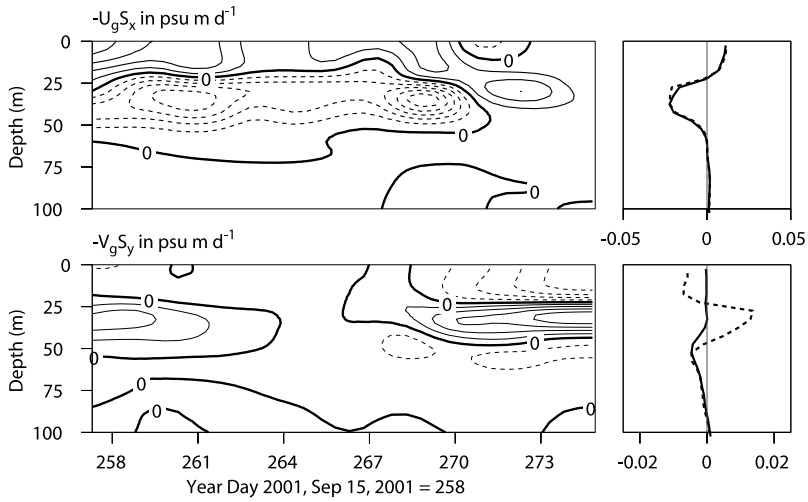

Figure 24. Vertical distribution of salinity advection per unit depth (psu m d^{-1}) by geostrophic velocity. Solid contours denote positive salinity fluxes, and dashed contours denote negative salinity fluxes (left panels). (top) Zonal advection and (bottom) meridional advection are both shown. The contour interval is 0.01 psu m d^{-1}. Cruise-averaged advection of salinity per unit depth (psu m d^{-1}) appears in the right panels. The short dashed line indicates the mean $\langle u_g\ \nabla S \rangle$, and the solid line indicates $\langle u_g \rangle$ $\langle \nabla S \rangle$.

Table 4a. Cruise-Averaged Horizontal Advection of Freshwater[a]

	0–20 m Layer				0–25 m Layer			
Horizontal Advection in Terms of mm d^{-1}	RB	NH	RB-NH	GV	RB	NH	RB-NH	GV
$D_1 = -\frac{1}{S_0}\int_{-h}^{0}\langle U\frac{\partial S}{\partial x}\rangle dz$	8.6	1.8	5.2	5.9	8.3	1.5	4.9	5.6
$D_2 = -\frac{1}{S_0}\int_{-h}^{0}\langle U\rangle\langle\frac{\partial S}{\partial x}\rangle dz$	7.4	6.0	6.7	5.5	7.4	6.0	6.7	5.5
$E_1 = -\frac{1}{S_0}\int_{-h}^{0}\left\langle V\frac{\partial S}{\partial y}\right\rangle dz$	−4.5	−1.2	−3.8	−3.8	−5.1	−2.1	−3.6	−4.1
$E_2 = -\frac{1}{S_0}\int_{-h}^{0}\langle V\rangle\left\langle\frac{\partial S}{\partial y}\right\rangle dz$	−0.9	−0.3	−0.6	−0.1	−1.8	−0.6	−1.2	−0.2
Total: $D_1 + E_1$	4	1	3	2	3	−1	1	2
Total: $D_2 + E_2$	7	6	7	5	6	5	6	5

[a]RB and NH denote flux estimates from the R/V *Ron Brown* ADCP and the R/V *New Horizon* ADCP, respectively. GV denotes flux estimates by use of geostrophic velocity. Cruise-averaged surface salinity was $S_0 = 33.6$ psu. Averages of RB and NH are given in the RB-NH column.

[72] The cruise-averaged precipitation minus evaporation ($P - E$) was estimated by summing all of the components of the freshwater budget (equation (3)) for the 0–20 and 0–25 m layers (Table 5). All of the terms were positive and of comparable magnitude for both of the layers except that turbulent freshwater flux at the base of the 25 m layer was small relative to the other components. Error estimates were computed in the same manner as for net surface heat flux (Table 3) and may be an underestimate, primarily because of neglecting uncertainty in vertical advection.

[73] The cruise averaged estimate of $P - E$ from the freshwater budget (Table 5) may be converted to a precipitation rate (P) by adding the evaporation rate (4.1 mm d^{-1} (Hare et al., submitted manuscript, 2005)) observed on the *Ron Brown*, which yields a precipitation rate of 29 mm d^{-1}. This value may be compared with other measurements during EPIC and with climatological estimates (Table 6). The freshwater budget value agrees well with ORG measurements on the *New Horizon* and the rainfall measurement on the *Ron Brown* from a combination of instruments [*Hare et al.*, 2002] and is in fair agreement with estimates from satellite microwave measurements. The ORG measurements on the *New Horizon* were reduced by 15% to correct for imperfect cosine response of the instrument [*Weller et al.*, 2004].

[74] Precipitation rate from the rain radar on the *Ron Brown* averaged over the cruise and a circle with 100 km radius was approximately one-third as large as the other estimates, which suggests that the formula used to convert radar reflectivity to precipitation rate may have been in error. The formula (Z-R relation) used to obtain the radar rainfall rates was $Z = 218\,R^{1.6}$, where Z is reflectivity in *dBZ* and R is the rainfall rate in mm h^{-1} (R. Cifelli and W. Peterson, http://olympic.atmos.colostate.edu/epic/rainmaps/README.pdf). The coefficients in the formula were based on precipitation data collected by the National Center for Atmospheric Research C-130 aircraft during the EPIC experiment. *Peterson et al.* [2003] estimated rainfall from the *Ron Brown* radar by use of two different Z-R relations one for stratiform and the other for convective rainfall; they cautioned that the appropriate Z-R relation for the EPIC region was uncertain.

[75] Rainfall rate from the *Ron Brown* radar averaged over the cruise illustrates the high degree of spatial variability in tropical rainfall (Figure 25). The average rainfall rate differed by as much as a factor of five at points separated by 150 km. The spatial variability illustrates the uncertainty in comparing point measurements separated in space, even if they are averaged over time, and in comparing measurements averaged over different regions. The average over a circle of 100 km radius given in Table 6 can be compared with averages with radii of 10 and 30 km, which yield rain rates of 16 and 14 mm d^{-1}, respectively [*Hare et al.*, 2002]. The best averaging radius for comparison with the estimate from the ocean budget is probably between 30 and 100 km, which would yield a mean rainfall rate of 13 mm d^{-1}, which is about half of the in situ and oceanic freshwater budget estimates (Table 6). The high degree of spatial variability in rainfall was also apparent in the cruise-averaged satellite estimates shown in Figure 2, where mean precipitation rate changed by nearly an order of magnitude over 150 km. The location of the maxima in satellite precipitation south of the butterfly pattern does not appear to agree with the location of the maxima from the *Ron Brown* radar (Figure 25). The difference may be due to intermittent sampling by the satellite, which may miss periods of heavy rainfall, and because rainfall estimates from microwave emission (cloud temperature) may not be perfectly correlated with rainfall rate.

5. Discussion and Summary

5.1. Regional Context

[76] To aid the interpretation of the EPIC heat and freshwater budgets it is useful to consider the regional structure of winds, currents, SST, and air-sea fluxes. The annual mean SST and precipitation fields are shown in

Table 4b. Cruise-Averaged Vertical Advection of Freshwater[a]

Vertical Advection in Terms of mm d^{-1}	0–20 m Layer	0–25 m Layer
$F_1 = -\frac{1}{S_0}\int_{-h}^{0}\langle W_E\frac{\partial S}{\partial z}\rangle dz$	0	1
$F_2 = -\frac{1}{S_0}\int_{-h}^{0}\langle W_E\rangle\langle\frac{\partial S}{\partial z}\rangle dz$	0	1.
$F_3 = -\frac{1}{S_0}\int_{-h}^{0}\langle W_M\rangle\langle\frac{\partial S}{\partial z}\rangle dz$	1.	4
$F_4 = -\frac{1}{S_0}\int_{-h}^{0}\langle W_A\rangle\langle\frac{\partial S}{\partial z}\rangle dz$	2	9

[a]The vertical salinity gradient was from SeaSoar data.

Table 5. Cruise-Averaged Freshwater Budget[a]

Terms in Equation (3), mm d^{-1}	0–20 m	0–25 m
Mean time rate of change, $-\frac{1}{S_0}\int_{-h}^{0}\langle\frac{\partial S}{\partial t}\rangle dz$; individual estimates from RB and NH are in brackets	+8 [8, 8]	+10 [9, 10]
Mean turbulent salt flux at depth h: $F_S(-h)$; standard error estimates are given in brackets	+11 [9, 13]	+3 [2, 3]
Total mean advection: [mean (D_2 + E_2)] + F_4; RB and NH estimates are in brackets	+9 [8, 9]	+15 [14, 15]
Horizontal advection bias correction	−3	−3
Net freshwater flux: *P-E*	+25 (±3)	+25 (±2)

[a]The quantities in brackets are upper and lower bounds from different estimates or, in the case of turbulent heat flux and the net freshwater flux, the approximate standard error estimate.

Figure 26. The center of the butterfly pattern was about three degrees of latitude north of the mean location of the ITCZ, which is shown as a band of maximum rainfall. The annual mean rainfall rate at the center of the butterfly pattern was 12 mm d^{-1}, compared to 16 mm d^{-1} about 300 km to the south at the center of the maxima in precipitation. The rain gauge and budget estimates of precipitation during the EPIC experiment were two to three times as large as the annual mean and the mean for September (Table 6), which is consistent with lower than normal near surface salinity during EPIC (Figure 5).

[77] Winds blowing through gaps in the Central American mountains cause striking variations in SST and ocean circulation within the eastern Pacific warm pool (Figure 26). The most prominent of these features is the Costa Rica dome, which is centered near 9°N, 90°W and has a surface expression of cool SST (<27.5 C) due to upwelling. The cool surface tends to suppress convection and, as a result, there is a minimum in precipitation coincident with the center of the dome (Figure 26). The band of relatively cool water extending toward the southwest from the dome is associated with a minimum in precipitation rate in the ITCZ at 90°W, presumably due to the relatively low SST.

5.2. Heat and Freshwater Budgets

[78] The 19 day averaged net surface heat flux computed from the heat budgets (equation (2)) of 0–20 m and 0–25 m oceanic layers (Table 3) is in good agreement with independent measurements at the center of the EPIC butterfly pattern. Mean surface heat flux from the ocean budget was 41 W m^{-2} (cooling) compared to 30 W m^{-2} from atmospheric measurements of the heat flux components (radiative, sensible and latent) from the ship at the center of the survey pattern (Hare et al., submitted manuscript, 2005). The difference between the two values is within the combined estimated error. The storage term dominated the heat budget and was positive (net cooling), which reflected mean surface cooling due to relatively low solar insolation (high cloudiness) coupled with relatively high evaporative cooling. Horizontal advection was a significant term in the heat budget and may have been enhanced by the presence of an anticyclonic eddy within the survey pattern. Horizontal advection tended to be compensated by vertical advection of cold water into the surface layers (Table 2). The estimated turbulent heat flux through the base of the oceanic layers was significant and of comparable magnitude to the penetrative solar radiation through the base (Table 3). The estimated long-term average net surface heat flux for the month of September from *da Silva et al.* [1994] is −28 W m^{-2} (heating), which indicates that the EPIC experimental period was anomalous.

[79] The 19 day mean *P-E* rate from the oceanic freshwater budgets (equation (3)) for the 20 and 25 m surface layers was 25 ± 3 mm d^{-1} for each layer (Table 5). All of the terms in the freshwater budget were significant and all were positive. The storage term was positive as the result of intermittent heavy rainfall during the experiment. The *P-E* rate was converted to an estimate of precipitation rate by adding the evaporation rate determined on the *Ron Brown* (Hare et al., submitted manuscript, 2005), which yielded a precipitation rate of 29 mm d^{-1}. This value is in excellent agreement with in situ measurements on the *New Horizon* and *Ron Brown* and in good agreement with satellite estimates (Table 6). Precipitation rates from the radar aboard the *Ron Brown* were one-third to one-half as large as the other estimates, depending on which averaging radius was

Table 6. Rainfall Estimates[a]

Method	Rain Rate, mm d^{-1}
Freshwater budget (averaged over a 146 × 146 km domain)	29
ORG:R/V *New Horizon* (averaged along the butterfly)	29
R/V *Ron Brown* (cruise-averaged near the center of the butterfly) [*Hare et al.*, 2002; Hare et al., submitted manuscript, 2005]	25
C-band Doppler radar [*Hare et al.*, 2002]	
Averaged over a circle of radius 10 km	16
Averaged over a circle of radius 100 km	11
TRMM TMI satellite rainfall: averaged over 1.5° × 1.5° area based on 3 day averaged, 0.25° × 0.25° gridded data (http://www.remss.com)	38
SSM/I satellite rainfall: averaged over 1.5° × 1.5° area based on 3 day averaged 0.25° × 0.25° gridded data (http://www.remss.com)	28
Climatology (GPCP [*Huffman et al.*, 1997]); TRMM TMI and PR data for the month of September (http://www.trmm.gsfc.nasa.gov)	10

[a]Evaporation rate, *E*, during the experiment was 4.1 mm d^{-1} (Hare et al., submitted manuscript, 2005), which was used to obtain *P* from the freshwater budget estimate of $P - E$ (Table 5). GPCP denotes Global Precipitation Climatology Project; PR denotes the precipitation radar on the TRMM satellite; SSM/I denotes special sensor microwave/imager. All estimates are averages over the cruise, except the last entry.

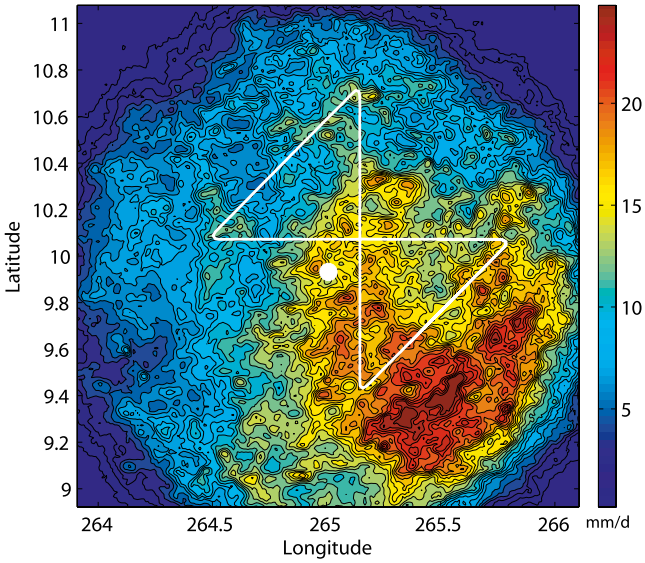

Figure 25. Cruise-averaged map of C-band radar rain rate from 12 September to 1 October 2001 (http://www.joss.ucar.edu/epic). The contour interval is 1 mm d^{-1}. The white bullet denotes the nominal location of the R/V *Ron Brown*, on which the radar was mounted. R/V *New Horizon*'s butterfly path is marked by white lines.

used. The rainfall radar estimates may be in error because of uncertainty in which formula should be used to convert measurements of radar backscatter to precipitation rate [*Peterson et al.*, 2003]. Apart from the rainfall radar, EPIC precipitation rates are about a factor of three larger than the climatological mean for the month of September (Table 6), which is consistent with the difference between the EPIC net heat flux (net surface cooling associated with high rainfall) and climatological net heat flux for September (net surface heating).

[80] The study revealed limitations of the ocean budget method for estimation of surface fluxes. The surface layer over which the budget is estimated needs to be sufficiently shallow to minimize errors due to unresolved motions in the pycnocline. The base of the layer should be deep enough to minimize turbulent fluxes through the base, i.e., turbulent fluxes should be sufficiently small that errors in their estimate do not seriously affect the budget. An uncertain aspect of ocean budget calculations is the difficulty in estimating vertical velocity. Several approaches were considered in this study and we chose the vertical velocity estimated from horizontal velocity divergence even though the uncertainty was large. This choice minimized the differences in surface flux estimates for the 20 and 25 m surface layers. The use of the conservation of mass equation for estimating vertical velocity in the pycnocline appeared to be a promising approach. In calculating horizontal advection it was necessary to correct for the bias in using the product of mean velocity and mean gradient (equations (2) and (3)) rather than the mean product of velocity and gradient. It may be advantageous to use geostrophic velocity rather than ADCP velocity for estimating advection because the geostrophic velocity minimizes the effect of tides and internal waves on the estimate.

[81] The strength of the ocean budget method for estimating precipitation was illustrated by this study. Low-salinity anomalies associated with the high degree of spatial and temporal variability in rainfall rate (Figures 4 and 25) tended to diffuse in the upper ocean; linear fits to salinity over the cross sections and over time smoothed the effects of the fluctuations that remained to yield a representative 19 day average.

5.3. Eastern and Western Pacific Warm Pools

[82] Results from the COARE experiment, particularly from the Intensive Flux Array (IFA) centered near 2°S, 156°E [*Webster and Lukas*, 1992; *Godfrey et al.*, 1998; *Feng et al.*, 1998b, 2000; *Weller et al.*, 2004], may be used to compare the role of the ocean in air-sea interaction processes in the eastern and western Pacific warm pools.

[83] This study illustrated that energetic anticyclonic ocean eddies may play an important role in the heat and freshwater budgets of the upper ocean in the eastern Pacific warm pool and that these eddies, which have positive SST anomalies, may be preferential sites for rainfall, as discussed below. Ocean eddies are less energetic in the western Pacific warm pool.

[84] The average depth of the actively mixing surface layer during the EPIC experiment was 12 m and the maximum was 28 m based on a density difference of 0.01 kg m^{-3} between the surface and the mixed layer

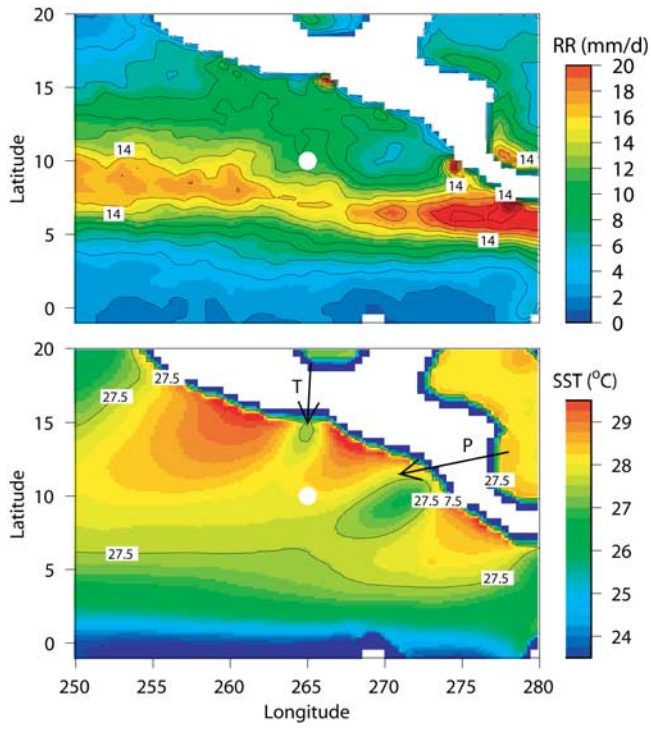

Figure 26. Six year (1998–2003) averaged TMI rain rate and SST derived from monthly averaged, 0.25° × 0.25° spatially gridded satellite data (http://www.remss.com). The white bullet shows the nominal location of the EPIC survey. Arrows marked in the SST panel show wind jets across the Isthmus of Tehuantepec (T) and the Gulf of Papagayo (P).

depth (Table 1). These values are relatively small even though there was evidence that mixing was more intense than the climatological mean for September. In contrast, the maximum depth of the actively mixing layer from the COARE IFA was 45 m during leg 1 [*Wijesekera and Gregg*, 1996], when winds were low and rainfall was light, and was 70 m during leg 2 [*Smyth et al.*, 1996] under the influence of a westerly wind burst.

[85] The pycnocline is relatively shallow and strong in much of the eastern Pacific warm pool. During the EPIC experiment the depth of the maximum vertical density gradient was 38 m and the buoyancy frequency at that depth was 23 h^{-1}. The corresponding values for the COARE IFA were 85 m and 14 h^{-1}. The depth of the pycnocline is variable over the eastern Pacific warm pool, primarily because of the variable effect of wind-driven upwelling. The depth is a minimum at the center of the Costa Rica dome where SST is also a minimum in the annual mean (Figure 26). Approximately 75% of the vertical density gradient in the seasonal pycnocline of the eastern Pacific warm pool is due to temperature. In the western Pacific warm pool there is sometimes a relatively shallow halocline or ''barrier layer'' [*Lukas and Lindstrom*, 1991] in conjunction with a relatively deep, nearly isothermal layer, called a ''thermostad.'' During the conditions of light rainfall, low winds, and relatively large downward net heat flux observed during leg 1 of COARE, the density step at the base of the mixed layer was dominated by temperature and there was a strong diurnal mixing cycle [*Wijesekera and Gregg*, 1996]. The long-term, vertical T and S profiles in the upper ocean of the COARE region are determined by small positive annual net surface heat flux, relatively large $P - E$, and sporadic westerly wind bursts. The relatively shallow thermocline over much of the eastern Pacific warm pool provides the potential for substantial changes in SST as the result of atmospheric forcing of entrainment at the base of the mixed layer. This is illustrated by the minimum in SST at the center of the Costa Rica dome, where upwelling and entrainment result in annual mean SST lower than 27.5°C (Figure 26).

[86] Inertial oscillations were the dominant internal wave motions during the EPIC experiment (Figure 6), unlike the COARE IFA in the western Pacific warm pool where the semidiurnal tide was dominant [*Feng et al.*, 1998a]. The long inertial period at the location (2°S) of the IFA tended to limit the development of inertial oscillations. The shallow mixed layer at the EPIC site contributed to large-amplitude inertial oscillations that produced strong shear in the pycnocline. This shear may have played an important role in mixing [*Gregg et al.*, 2002].

5.4. High Rainfall Over a Warm Eddy

[87] The approximate colocation, within and near the butterfly pattern, of an anticyclonic eddy with relatively high SST and heavy rainfall (Figure 2) may be more than a chance occurrence. In the discussion below we advance the hypothesis that anticylonic eddies, which form in warm water near the Central American coast, move westward with high SST anomalies and are preferential sites for atmospheric convection and heavy rainfall.

[88] *Giese et al.* [1994] used satellite altimeter data to describe anticyclonic eddies that form near the Central American coast and propagate westward at a speed of about 0.17 m s^{-1} in the latitude band from 10° to 12°N. The anticyclonic eddies are thought to be generated by wind jets that flow through the gaps in the Central American mountains and continue across the Gulfs of Tehuantepec and Papagayo (Figure 26). The generation is caused by negative wind stress curl on the right sides of the wind jet vectors [*McCreary et al.*, 1989]. Negative wind stress curl forces surface convergence, downwelling, and, through conservation of vorticity, anticyclonic rotation. Warm water in the generation regions (Figure 26) is incorporated into the eddies and their surface becomes a positive SST anomaly as they move westward into cooler ambient water (Figure 26). The interaction of the NECC and the Central American coast may also play a role in the generation of anticyclonic eddies [*Hansen and Maul*, 1991].

[89] The daily-averaged SST within the butterfly pattern at the beginning of the experiment was near 29.5°C with daytime values reaching 31°C (Figure 11). There was a maximum (30.5°C) in satellite (TMI) SST located 140 km southwest of the center of the butterfly pattern and averaged over the 3 days ending on year day 263. This maximum is not shown here but it was located near the southern edge of the broad cruise-averaged maximum in SST shown in Figure 2. The location of the SST maximum does not match the location of the maximum in sea surface height (SSH (Figure 2)), perhaps because there is uncertainty in the SSH field and because SST may not be perfectly colocated with the center of the eddy. Near-surface velocity measured near the center of the butterfly (Figure 8) was consistent with the westward movement of an anticyclonic eddy past the center, suggesting that the precise location of the eddy from the SSH field was in error. The location of the maximum in SST on year day 263 was close to the location of the cruise-averaged maximum in average rainfall measured by the rain radar on the *Ron Brown* (Figure 25). Both maxima were southwest of the butterfly center and were not more than 50 km apart. We suggest that the maximum in cruise-averaged rainfall may have been caused by the underlying maximum in SST, which was associated with an anticyclonic eddy.

[90] In further support of the hypothesis that anticyclonic eddies with high SST anomalies are preferential sites for atmospheric convection, there appears to be a qualitative correlation between cruise-averaged SST, sea surface height anomalies, and rainfall rate at locations other than the butterfly pattern and its vicinity (Figure 2). There appears to be a positive correlation between the SST maximum at 13°N, 262°E and SSH and rainfall rate near the same location (Figure 2). There also appears to be a correlation between relatively high SST centered near 12°N, 270°E, the three anticyclonic eddies in the vicinity of the same point, and a broad maximum in rainfall rate over the same area. Similar correlation is found at 9°N, 274°E near the edge of Figure 2. The correlation is not perfect, perhaps partly because of the noise in the SSH field. Research on the hypothesis advanced here is in progress.

[91] **Acknowledgments.** For assistance aboard the R/V *New Horizon*, we are indebted to K. Wagner and the SIO SeaSoar group, C. Matson, S. Rusk, F. Delahoyde, and R. Patrick. We are grateful to the

master and crew of the R/V *New Horizon* for their contributions to a successful cruise and to J. Wagner, J. Simpkings, and A. Erofeev for assisting in preparations for the cruise. We are thankful to C. Fairall and F. Bradley for sharing meteorological data, to R. Cefelli and the Colorado State University rain-radar group for providing radar rainfall estimates, to D. Chelton for providing satellite temperature and wind stress fields, and to T. Strub and C. James for providing their satellite altimeter data sets. This work was supported by National Science Foundation grants OCE-0002758 (for C.A.P. and H.W.W.) and OCE-0002598 (for D.L.R.). Comments by anonymous reviewers and Ragu Murtugudde are greatly appreciated.

References

Candela, J., R. C. Beardsley, and R. Limeburner (1992), Separation of tidal and subtidal currents in ship-mounted acoustic Doppler current profiler observations, *J. Geophys. Res.*, *97*, 769–788.

Chelton, D. B., M. H. Freilich, and S. K. Esbensen (2000), Satellite observations of the wind jets off the Pacific coast of Central America. part I: Case studies and statistical characteristics, *Mon. Weather Rev.*, *128*, 1993–2018.

Clarke, A. J. (1988), Inertial wind path and sea surface temperature patterns near the Gulf of Tehuantepec and Gulf of Papagayo, *J. Geophys. Res.*, *93*, 15,491–15,501.

Cronin, M. F., N. Bond, C. Fairall, J. Hare, and M. J. McPhaden (2002), Enhanced oceanic and atmospheric monitoring underway in eastern Pacific, *Eos Trans. AGU*, *83*, 205, 210–211.

da Silva, A., A. C. Young, and S. Levitus (1994), *Atlas of Surface Marine Data 1994*, vol. 1, *Algorithms and Procedures*, *Tech. Rep. 6*, U.S. Dep. of Comm., Washington, D. C.

Efron, B., and G. Gong (1993), A leisurely look at the bootstrap, the jackknife, and cross-validation, *Am. Stat.*, *37*, 36–48.

Fairall, C. W., E. F. Bradley, D. P. Rogers, J. B. Edson, and G. S. Young (1996), Bulk parameterization of air-sea fluxes for tropical ocean-global atmospheric coupled-ocean response experiment, *J. Geophys. Res.*, *101*, 3747–3764.

Feng, M., M. A. Merrifield, R. Pinkel, P. Hacker, A. J. Plueddemann, E. Firing, and R. Lukas (1998a), Semidiurnal tides observed in the western equatorial Pacific during the Tropical Ocean-Global Atmosphere Coupled Ocean-Atmosphere Response Experiment, *J. Geophys. Res.*, *103*, 10,253–10,272.

Feng, M., P. Hacker, and R. Lukas (1998b), Upper-ocean heat and salt balances in response to a westerly wind burst in the western equatorial Pacific during TOGA COARE, *J. Geophys. Res.*, *103*, 10,289–10,311.

Feng, M., R. Lukas, P. Hacker, R. A. Weller, and S. P. Anderson (2000), Upper-ocean heat and salt balances in the western equatorial Pacific in response to the intra-seasonal oscillation during TOGA COARE, *J. Clim.*, *13*, 2409–2427.

Fiedler, P. C. (2002), The annual cycle and biological effects of the Costa Rica Dome, *Deep Sea Res., Part I*, *49*, 321–338.

Giese, B. J., J. A. Carton, and L. J. Holl (1994), Sea level variability in the eastern tropical Pacific as observed by TOPEX and tropical ocean–global atmosphere tropical atmosphere-ocean experiment, *J. Geophys. Res.*, *99*, 24,739–24,784.

Godfrey, J. S., R. A. Houze Jr., R. H. Johnson, R. Lukas, J.-L. Redelsperger, A. Sumi, and R. Weller (1998), Coupled Ocean-Atmosphere Response Experiment (COARE): An interim report, *J. Geophys. Res.*, *103*, 14,395–14,450.

Gregg, M. C., J. Mickett, G. Carter, and D. Winkel (2002), Mixing and shear at 10°N, 95°W during EPIC 2001, *Eos Trans. AGU*, *83*(47), Fall Meet. Suppl., Abstract A21D-07.

Hansen, D. V., and G. A. Maul (1991), Anticyclonic current rings in the eastern tropical Pacific ocean, *J. Geophys. Res.*, *96*, 6965–6979.

Hare, J., F. Bradley, and C. W. Fairall (2002), Rainfall measurements on the R/V *Ronald H. Brown* during EPIC 2001, *Eos Trans. AGU*, *83*(47), Fall Meet. Suppl., Abstract A22A-0059.

Hofmann, E. E., A. J. Busalacchi, and J. J. O'Brien (1981), Wind generation of the Costa Rica Dome, *Science*, *241*, 522–554.

Huffman, G. J., R. F. Adler, P. Arkin, A. Chang, R. Ferraro, A. Gruber, J. Janowiak, A. McNab, B. Rudolf, and U. Schneider (1997), The global precipitation climatology project (GPCP) combined precipitation data set, *Bull. Am. Meteorol. Soc.*, *78*, 5–20.

Kessler, W. S. (2002), Mean three-dimensional circulation in the northeast tropical Pacific, *J. Phys. Oceanogr.*, *32*, 2457–2471.

Levitus, S. (1982), Climatological atlas of the world ocean, *NOAA Prof. Pap.*, *13*, 173 pp.

Lukas, R. S., and E. Lindstrom (1991), The mixed layer of the western equatorial Pacific Ocean, *J. Geophys. Res.*, *96*, 3343–3357.

McCreary, J. P., H. S. Lee, and D. B. Enfield (1989), The response of the coastal ocean to strong off shore winds: With application to circulations in the Gulfs of Tehuantepec and Papagayo, *J. Mar. Res.*, *47*, 81–109.

Mitchell, T. P., C. Deser, and J. M. Wallace (1989), The influence of sea surface temperature on surface wind in the eastern equatorial Pacific: Seasonal and interannual variability, *J. Clim.*, *2*, 1500–1506.

Muller-Karger, F. E., and C. Fuentes-Yaco (2000), Characteristics of wind-generated rings in the eastern tropical Pacific Ocean, *J. Mar. Res.*, *105*, 1271–1284.

Ohlmann, J. C. (2003), Ocean radiant heating in climate models, *J. Clim.*, *16*, 1337–1351.

Osborn, T. R. (1980), Estimates of the local rate of vertical diffusion from dissipation measurements, *J. Phys. Oceanogr.*, *10*, 83–89.

Paulson, C. A., and J. J. Simpson (1970), Irradiance measurements in the upper ocean, *J. Phys. Oceanogr.*, *7*, 953–956.

Payne, R. E. (1972), Albedo of the sea surface, *J. Atmos. Sci.*, *39*, 959–970.

Peterson, W. A., R. Cifelli, D. J. Boccippio, S. A. Rutledge, and C. Fairall (2003), Convection and easterly wave structures observed in the eastern Pacific warm pool during EPIC-2001, *J. Atmos. Sci.*, *60*, 1754–1773.

Pollard, R. T., and L. A. Regier (1992), Vorticity and vertical circulation at an ocean front, *J. Phys. Oceanogr.*, *22*, 609–625.

Raymond, D. J., S. E. Esbensen, C. A. Paulson, M. C. Gregg, C. S. Bretherton, W. A. Petersen, R. Cifelli, L. K. Shay, C. Ohlmann, and P. Zuidema (2004), EPIC 2001 and the coupled ocean-atmosphere system of the tropical east Pacific, *Bull. Am. Meteorol. Soc.*, *85*, 1341–1354.

Serra, Y. L., and R. A. Houze Jr. (2002), Observations of variability on synoptic timescales in the east Pacific ITCZ, *J. Atmos. Sci.*, *55*, 2763–2781.

Shay, L. K., T. M. Cook, S. D. Jacob, C. Zhang, and M. McGauley (2002), Airborne expendable current, temperature and salinity profiling in EPIC, *Eos Trans. AGU*, *83*(47), Fall Meet. Suppl., Abstract A22A-0069.

Smyth, W. D., D. Hebert, and J. N. Moum (1996), Local ocean response to a multiple westerly wind burst: 1. Dynamic response, *J. Geophys. Res.*, *101*, 22,495–22,512.

Strub, P. T., and C. James (2000), Altimeter-derived variability of surface velocities in the California current system: 2. Seasonal and eddy statistics, *Deep Sea Res., Part II*, *47*, 831–870.

Umatani, S., and T. Yamagata (1991), Response of the eastern tropical Pacific to meridional migration of the ITCZ: The generation of the Costa Rica Dome, *J. Phys. Oceanogr.*, *21*, 363–364.

Webster, P. J., and R. Lukas (1992), TOGA COARE: The Coupled Ocean-Atmosphere Response Experiment, *Bull. Am. Meteorol. Soc.*, *73*, 1377–1416.

Weller, R. A., F. Bradley, and R. Lukas (2004), The interface or air-sea flux component of the TOGA Coupled Ocean-Atmosphere Response Experiment and its impact on subsequent air-sea interaction studies, *J. Oceanic Atmos. Technol.*, *21*, 223–257.

Wijesekera, H. W., and M. C. Gregg (1996), Surface layer response to weak winds, westerly bursts, and rain squalls in the western Pacific Warm Pool, *J. Geophys. Res.*, *101*, 977–997.

Wyrtki, K. (1964), Upwelling in the Costa Rica Dome, *Fish. Bull.*, *63*, 355–372.

Xie, S.-P., H. Xu, W. S. Kessler, and M. Nonaka (2005), Air-sea interaction over the eastern Pacific warm pool: Gap winds, thermocline dome, and atmospheric convection, *J. Clim.*, *18*, 5–25.

M. C. Gregg and J. Mickett, Applied Physics Laboratory, University of Washington, 1013 NE 49th Street, Seattle, WA 98105-6698, USA. (gregg@apl.washington.edu; mickett@apl.washington.edu)

C. A. Paulson, S. D. Pierce, and H. W. Wijesekera, College of Oceanic and Atmospheric Sciences, 104 Ocean Administration Building, Burt Hall, Room 320, Oregon State University, Corvallis, OR 97331-5503, USA. (cpaulson@oce.orst.edu; spierce@coas.oregonstate.edu; hemantha@coas.oregonstate.edu)

W. S. Pegau, Kachemak Bay Research Reserve, 95 Sterling Highway, Suite 2, Homer, AK 99603, USA. (scott_pegau@fishgame.state.ak.us)

D. L. Rudnick, Scripps Institution of Oceanography, University of California, San Diego, Mail Code 0213, La Jolla, CA 92093-0213, USA. (drudnick@ucsd.edu)